The Astrophysical Journal, 939:9 (22pp), 2022 November 1 https://doi.org/10.3847/1538-4357/ac94c7

A Comparison of Global Magnetofrictional Simulations of the 2015 March 20 Solar Eclipse

Duncan H. Mackay[1] and L. A. Upton[2]
[1] School of Mathematics and Statistics, University of St Andrews, North Haugh, St Andrews, Fife KY16 9SS, UK; dhm@st-and.ac.uk
[2] Southwest Research Institute, 1050 Walnut St, Suite 300, Boulder, CO 80302, USA
Received 2022 April 5; revised 2022 August 23; accepted 2022 September 22; published 2022 October 27

Abstract

The solar corona exhibits a wide range of phenomena, from highly non-potential objects such as solar filaments to near-potential structures such as the open magnetic flux. For any global model to be useful in space weather applications, the model must on a single day reproduce all of these phenomena in the same simulation, using the same set of coronal physics and parameters. The purpose of the present paper is to evaluate whether the evolving magnetofrictional model can achieve this goal. Twenty-eight separate simulations are analyzed, where each tries to reproduce both highly non-potential and near-potential phenomena observed in the solar corona on the same day. This day is chosen to be 2015 March 20, the date of the solar eclipse. The study evaluates how the cadence of bipole data, ideal or nonideal coronal physics, and the variety of helicity injection mechanisms affect the accuracy of the simulations. Results show that significantly better agreement arises when using Advective Flux Transport (AFT) synoptic maps to drive the simulations, as compared to 27-day Carrington rotation synoptic maps. Using the nonideal effect of hyperdiffusion leads to the worst agreement with all coronal phenomena. Alternatively, when running either ideal or ohmic diffusion simulations with helicity condensation or bipoles with a self-helicity, a good agreement with both on-disk and limb structures can be found. This suggests that future studies aiming to simulate the corona and reproduce multiple phenomena on a given day should use data products such as AFT and avoid using the nonideal physics of hyperdiffusion.

Unified Astronomy Thesaurus concepts: Solar corona (1483); Solar magnetic fields (1503); Solar evolution (1492); Solar prominences (1519)

1. Introduction

In the paper of Yeates et al. (2018), a comparison of global non-potential models was presented. A wide variety of models were considered, including nonlinear force-free field (NLFFF) extrapolations (Wiegelmann 2007; Amari et al. 2013), magnetohydrostatic extrapolations (Bogdan & Low 1986; Wiegelmann et al. 2020), force-free electrodynamic techniques (Contopoulos et al. 2011; Contopoulos 2013), an evolving magnetofrictional model (Mackay & van Ballegooijen 2006a; Yeates 2014), and MHD models (Mikic & Linker 1994; Mikic et al. 1999; Feng et al. 2012). The various coronal structures produced by each model were compared to one another and to coronal observations taken on 2015 March 20, the date of the solar eclipse. While some common features were found between the models, due to the variety of approaches applied, along with the varying use of observed boundary conditions, a wide range of solutions were obtained. One key difference in the use of the boundary conditions was that all of the models, except for the evolving magnetofrictional model, used a static boundary condition. This boundary condition was derived from a composite of two successive Solar Dynamic Observatory/Helioseismic and Magnetic Imager (SDO/HMI; Scherrer et al. 2012) synoptic maps (see Figure 2 of Yeates et al. (2018)). While the static models used this composite synoptic map, each approach processed the map in a different way, leading to a variety of boundary conditions (see Figure 3 of Yeates et al. (2018)). Another difference was that some approaches used the full vector field, while others used just the radial field component. Full details of the models and applied boundary conditions can be found in Table 1 of Yeates et al. (2018).

The focus of the present paper is to consider in more detail the evolving magnetofrictional solution presented in Yeates et al. (2018). The magnetofrictional model has many well-constrained parameters such as the flow velocities and diffusion coefficient used in the surface flux transport model (Sheeley 2005) or the use of ideal magnetofriction (Yang et al. 1986) to relax the corona toward a NLFFF state. It also has a number of terms that can be varied, such as the observational inputs used to drive the simulations and the coronal terms used to follow the subsequent response of the corona. Due to this, the single solution presented in Yeates et al. (2018) represented only one possible solution, derived from a particular set of parameters and physical effects. It is therefore important to consider the robustness of this solution along with determining how it may change as the terms and input data are varied.

The present paper will therefore carry out a detailed analysis of the variety of global solutions that can be produced from the model of Mackay & van Ballegooijen (2006a) and Yeates (2014). This will determine if a single set of parameters or physical effects can be determined that best reproduce the wide range of potential and non-potential structures found in the corona. These structures range from relatively low-lying but highly non-potential fields such as solar filaments, to radially extended near-potential coronal loops seen at the solar limb—and subsequently the amount and distribution of open flux (Linker et al. 2017). The present comparison follows the same principle as Yeates et al. (2018), where the simulations and observations are compared at a fixed point in time. This is again

taken to be the day of the solar eclipse on 2015 March 20. This not only allows the variability of the solutions from the evolutionary magnetofrictional model to be studied, but it will also determine if there is a single set of coronal physics and parameters that allows the model to reproduce both the potential and non-potential phenomena found on the Sun. In addition, the variety of solutions produced by the global magnetofrictional model can be compared to the other modeling approaches in Yeates et al. (2018). In the recent paper of Wagner et al. (2022), a study with similar goals was carried out using the EUHFORIA model (Pomoell & Poedts 2018). In the EUHFORIA model, the applied Schatten Current Sheet height (R_{scs}, Schatten 1971) and Potential Field Source Surface height (R_{SS}) were varied for two solar eclipses in 2008 and 2010. Through using both EUV and white light data from multiple perspectives and sources, along with a mixture of visual inspection and metric evaluation, the authors were able to obtain a unique combination of R_{scs} and R_{SS} that fitted their observations on both days.

One of the most important aspects of the global magnetofrictional method of Mackay & van Ballegooijen (2006a) and Yeates (2014) is the source function used to specify the emergence of new bipolar active regions across the Sun. This allows the surface field to remain accurate over extended periods of time so that observed distributions may be reproduced from one rotation to the next. For the vast majority of previous applications of the model (Yeates et al. 2008; Yeates 2014), the bipoles used to drive the simulations have been determined from Carrington Rotation (CR) synoptic magnetograms. As such, the properties of new bipoles are only identified once every 27 days, as they pass through central meridian. This means that, in the model, new flux emerges at each longitude only once per 27 days. While this approach has been successful in reproducing the overall structure of the large-scale field, it is not clear how well it can reproduce a wide variety of structures found across the solar disk and on the solar limb on a given day. This will be evaluated in the present study.

As an alternative to using Carrington rotation maps for determining the bipoles, in recent years a new data-driven modeling technique for photospheric magnetic fields, called Advective Flux Transport (AFT), has been developed by Upton & Hathaway (2014a, 2014b) to produce global maps of the Sun's magnetic field with a cadence of up to 15 s. AFT is able to operate in two modes: the Baseline mode and the Predictive mode. In the Baseline mode, AFT continuously assimilates magnetograms (nominally every 96 minutes for MDI and hourly for HMI). The AFT Baseline combines data assimilation with magnetic flux transport to produce maps with an instantaneous representation of the Sun's radial magnetic field over the entire surface. In the Predictive mode, AFT begins with the most recently available Baseline map and synthetic active regions (with observed properties) are incorporated into the model in order to make forecasts of the magnetic field evolution.

In the present study, we will consider for the first time what differences arise in the accuracy of the coronal field when the higher-cadence instantaneous AFT Baseline maps at a cadence of 1 hr are used instead of standard 27-day daily synoptic maps for determining the source function for new emerging bipoles. Due to the long-term nature of the present simulations, 1 hr AFT data is more than sufficient when comparing results to 27-day Carrington rotation maps. One fundamental difference between AFT maps and standard daily synoptic maps (also known as Carrington rotation maps) is that the data assimilation process allows AFT to regularly update the model with the near-side magnetic field from the latest magnetogram observations. This means that new bipoles emerge across all visible longitudes (both pre- and post-central meridian). While some daily synoptic maps (e.g., HMI Daily Update Synchronic Frames) do incorporate the observations within $+/-60^{\circ}$ in longitude, active regions outside of that window are neglected entirely. This includes far-side active regions, which appear as they did when they were last observed, as much as two weeks prior. In AFT, however, far-side active regions continue to evolve via observed flux transport processes.

While the accuracy of the photospheric field in the model of Mackay & van Ballegooijen (2006a) and Yeates (2014) is one aspect of the global modeling technique, another is the variety of coronal physics and helicity injection mechanisms that the model applies. In past studies, the coronal physics has used either ideal assumptions (Mackay & van Ballegooijen 2001; Mackay et al. 2018) or simulations involving nonideal effects such as ohmic diffusion (Mackay & van Ballegooijen 2006a; Yeates & Mackay 2009) or hyperdiffusion (Yeates & Mackay 2012; Yeates 2014; Mackay et al. 2016; Bhowmik & Yeates 2021). In addition to this, a variety of helicity injection mechanisms have been used. While helicity injection from the surface motions of differential rotation and meridional flow are common to all studies using this model, additional mechanisms may include either the self-helicity of the bipole (Yeates et al. 2008) or a large-scale representation of the helicity condensation process of Antiochos (2013), called the statistically averaged helicity condensation (SAHC) model (Mackay et al. 2014). The consequences of applying each of these effects on reproducing coronal structures on a given date will also be tested in this study. While the models of Mackay & van Ballegooijen (2006a) and Yeates (2014) have used a variety of helicity injection mechanisms, it should be noted that other studies have estimated the helicity injection over active region scales through the direct inversion of observational data: see, e.g., Mackay et al. (2011), Gibb et al. (2014), Kazachenko et al. (2014), Kazachenko et al. (2015), Lumme et al. (2017), and Yardley et al. (2021).

This paper is structured as follows. In Section 2, the global magnetofrictional model is described along with the determination of magnetic bipoles from both AFT and SDO/HMI synoptic magnetograms. The comparison of the simulations is carried out in Section 3, where a total of 28 separate simulations are analyzed and compared with a variety of observed coronal structures. Finally, the results are discussed in Section 4, along with the determination of the optimal simulation parameters for reproducing the solar corona on 2015 March 20, the day of the solar eclipse.

2. Magnetofrictional Simulations, Bipole Input Data, and Initial Conditions

To simulate the global non-potential coronal magnetic field of the Sun on the date of the solar eclipse in 2015 March, we apply the magnetofrictional evolutionary model of Mackay & van Ballegooijen (2006a) and Yeates (2014). The model simulates the continuous evolution of both the photospheric and coronal magnetic fields, as the coronal field evolves through a continuous series of quasi-static nonlinear force-free

states. These states are produced in response to photospheric boundary driving and magnetic flux emergence. To simulate the photospheric and coronal magnetic fields on the date of the eclipse, the simulations start on 2014 September 1 and run until 2015 March 30 (210 days). An extended period of time prior to the eclipse is simulated, so that non-potential effects may have time to self-consistently build up (Yeates et al. 2008), prior to the comparison of the various simulations with the observations. The 3D evolutionary model is described in Section 2.1, along with the variety of physical effects that may be included. In Section 2.2, the determination and properties of the high- and low-cadence bipole data sets used to drive the simulations are described. Finally, the initial condition applied to each of the simulations is discussed in Section 2.3.

2.1. Global Magnetofrictional Model

For the non-potential simulations, the Sun's 3D magnetic field,

$$\boldsymbol{B}(r,\,\theta,\,\phi,\,t) = (B_r,\,B_\theta,\,B_\phi) = \nabla \times \boldsymbol{A}, \tag{1}$$

is considered in the domain $r = [R_\odot,\,2.5R_\odot]$, $\theta = [0,\,\pi]$, and $\phi = [0,\,2\pi]$, where it is expressed in terms of $\boldsymbol{A}$, the magnetic vector potential. The evolution of the 3D magnetic field is driven by photospheric ($r = R_\odot$) boundary flows combined with magnetic flux emergence. This boundary driving using the magnetic flux transport model described in Mackay & van Ballegooijen (2006a) and Yeates (2014) produces a continuously evolving radial magnetic field, $B_r(R_\odot,\,\theta,\,\phi,\,t)$, over extended periods of time. At $r = R_\odot$, the magnetic flux transport process is given by

$$\frac{\partial \boldsymbol{A}_s}{\partial t} = \boldsymbol{v}_s \times \boldsymbol{B}_r - D\boldsymbol{\nabla}_s \times \boldsymbol{B}_r + \boldsymbol{S}_b, \tag{2}$$

where $\boldsymbol{A}_s$ is the magnetic vector potential tangent to the solar surface, $\boldsymbol{v}_s$ is the surface velocity of differential rotation (Snodgrass 1983) and meridional circulation (Duvall 1979), $D = 450$ km^{2}s^{-1} is the supergranular diffusion coefficient, and $\boldsymbol{\nabla}_s$ is the curl operator including only tangential (latitude and longitude) components. Supergranular diffusion models the large-scale consequences of the random walk of small-scale flows such as supergranulation on the photospheric magnetic field (Leighton 1964). The functional form used for differential rotation and meridional flow along with their assumed parameters are given in Mackay et al. (2014). The final term in Equation (2) represents the source function for magnetic flux emergence of large magnetic bipoles. This term is specified at fixed points in time using the bipole data set properties described in Section 2.2.

In response to the above boundary motions at the solar photosphere, the magnetic field in the coronal volume evolves through a continuous sequence of NLFFF states using a magnetofrictional relaxation technique (van Ballegooijen et al. 2000; Mackay & van Ballegooijen 2006a). The magnetic field follows the uncurled induction equation,

$$\frac{\partial \boldsymbol{A}}{\partial t} = \boldsymbol{v} \times \boldsymbol{B} + \boldsymbol{R}, \tag{3}$$

where $\boldsymbol{v}(\boldsymbol{r},\,t)$ is the plasma velocity in the corona and $\boldsymbol{R}$ represents a variety of optional physics that may be included. Optional terms include the nonideal processes of ohmic dissipation and hyperdiffusion or the ideal process of helicity condensation (Antiochos 2013). For the magnetofrictional relaxation technique (Yang et al. 1986), the coronal velocity is given by

$$\boldsymbol{v} = \frac{1}{\nu}\frac{\boldsymbol{j} \times \boldsymbol{B}}{B^2} + v_o e^{-(2.5R_\odot - r)/r_w}\hat{\boldsymbol{r}}, \tag{4}$$

where $\boldsymbol{j} = \nabla \times \boldsymbol{B}$, $v_o = 100$ km s^{-1}, $r_w = 0.1R_\odot$, and $\nu = 5dt/(r\sin\theta d\phi)^2$ is the frictional coefficient. The first term describes the "frictional" term, which acts when boundary motions depart the coronal field from a force-free equilibrium state. The resulting magnetic force then acts to return the field to a force-free state (generally, a nonlinear force-free field). This approximation may be used in a low beta plasma, when we are interested in long-lived structures of the coronal field and the boundary motions are slow compared to the coronal Alfvén speed. The second term represents a radial outflow velocity imposed to ensure that the field lines remain radial at the source surface ($R_{ss} = 2.5R_\odot$). This velocity simulates the effect of the solar wind in opening coronal field lines. In a recent paper, Rice & Yeates (2021) have developed a new method for constructing a global coronal equilibrium that includes a solar wind outflow velocity. Full details of the applied boundary conditions and numerical grid can be found in Section 2.1 of Mackay et al. (2014).

The second term on the right-hand side of Equation (3) represents the optional ideal and nonideal process that may be applied to the simulations. It is given by

$$\boldsymbol{R} = \eta_c \boldsymbol{j} + \frac{\boldsymbol{B}}{B^2}\nabla \cdot (\eta_4 B^2 \nabla \alpha) + \boldsymbol{H}_{sg}, \tag{5}$$

where

$$\eta_c = \eta_o\left(1 + 0.2\frac{|\boldsymbol{j}|}{B}\right), \tag{6}$$

$$\alpha = \frac{\boldsymbol{B} \cdot \nabla \times \boldsymbol{B}}{B^2}, \tag{7}$$

and

$$\boldsymbol{H}_{sg} = \begin{cases} \nabla_r(\zeta B_r), & r = R_\odot; \\ 0, & \text{otherwise.} \end{cases} \tag{8}$$

$$\zeta \equiv \overline{l^2\omega_l}/2, \tag{9}$$

The first term on the right-hand side of Equation (5) represents ohmic dissipation, which includes both a background term (η_o) and an enhanced term that acts in regions of strong current density. The enhanced term mainly acts when twisted flux rope structures are produced and limits the amount of twist within them by decreasing the amount of poloidal flux (Mackay & van Ballegooijen 2006a). The second term describes hyperdiffusion (Boozer 1986; Strauss 1988; Bhattacharjee 1995), a higher-order form of diffusion that allows total magnetic helicity to be conserved (van Ballegooijen & Mackay 2007) as the magnetic field relaxes toward a linear force-free state (Taylor 1974). The third term in Equation (3) represents the Statistically Averaged Helicity Condensation (SAHC) model (Equations (8) and (9)), which is a temporally and spatially averaged, statistical approximation to the process of helicity condensation (Antiochos 2013). Within the present study, only this large-scale

representation of the helicity condensation process is applied, as it is presently not possible to resolve flows on the scale of granules or super-granules in 3D global simulations that couple the photosphere and corona. The SAHC model is described in detail in the papers of Mackay et al. (2014, 2018), where ∇_r is the gradient operator including only the radial derivative and the parameter ζ controls the rate and scale of the helicity injection at the photosphere. The over-line denotes a spatial and temporal average over the characteristic scales of convection where l and ω_l are the radius and vorticity within the convection cells. This term has the effect of twisting the footpoints of the coronal magnetic field at the photosphere, which in turn inject a horizontal twist component into the magnetic field at the base of the corona. Once injected, this twist propagates upward into the corona along the field lines. The global consequences of the SAHC model in conjunction with other large-scale helicity injection mechanisms has been discussed in the papers of Mackay et al. (2014, 2018).

For the present study, both ideal and nonideal simulations and those with and without the SAHC model will be compared. When nonideal simulations are considered, only one of either ohmic or hyperdiffusion will be applied. The parameters used in the present study are similar to those used in previous studies, where the nonideal terms have values of $\eta_o = 60$ km^{2}s^{-1} (Mackay & van Ballegooijen 2006a) and $\eta_4 = 1 \times 10^{11}$ km^{4}s^{-1} (van Ballegooijen & Mackay 2007; Yeates 2014; Mackay et al. 2016). With this, the ratio of the hyperdiffusion timescale to that of ohmic diffusion $\tau_{HD}/\tau_O \sim 290$, suggesting that hyperdiffusion should have significantly less effect. Upon comparing the magnitude of hyperdiffusion used in the present study to that of Karna et al. (2021), it should be noted that the value used here is nine orders of magnitude smaller. The implications of this will be discussed in Section 3. For the SAHC model, the parameters are set to be $\bar{l} = 20,000$ km and $|\overline{\omega_l}| = 1 - 5 \times 10^{-6}$ s^{-1} (Mackay et al. 2014, 2018), where the parameter ζ ranges from approximately 200 to 1000 km^2 s^{-1}. As with previous studies, the angular rotation rate is assumed to be spatially uniform in each hemisphere, but with the sign changing across the equator. Positive/negative values of vorticity are used in the northern/southern hemisphere to inject negative/positive helicity.

2.2. Bipole Properties

To compare the global simulations with the observations, the radial magnetic field at the solar photosphere must reproduce as accurately as possible the observed distributions found on the Sun. Due to the continuous nature of the simulations, this must occur throughout the entire duration of the simulation from its start date (2014 September 1) to the date of the eclipse (2015 March 20). A key element for maintaining the accuracy of the simulations over long periods of time is the emergence of new bipolar active regions with properties determined from observed magnetograms. In the present simulations, new bipoles are inserted in an idealized form, both at the photosphere and in the corona. Idealized bipoles are used because their field needs to be specified at both the photosphere and in the corona. In the present simulations, the 3D mathematical form of each bipole in terms of the local coordinate system (x, y, z) relative to its center point is

$$B_x = B_0 e^{0.5}\left(\frac{z}{\rho_0}e^{-\xi} + 4\beta\frac{xy}{\rho_0^2}e^{-2\xi}\right),$$

$$B_y = 2\beta B_0 e^{0.5}\left(1 - \frac{x^2+z^2}{\rho_0^2}\right)e^{-2\xi},$$

$$B_z = B_0 e^{0.5}\left(-\frac{x}{\rho_0}e^{-\xi} + 4\beta\frac{yz}{\rho_0^2}e^{-2\xi}\right),$$

where ρ_0 is the half separation between the peaks of the bipole, $B_0 = \Phi/(\sqrt{\pi e}\,\rho_0^2)$ is the peak flux density, Φ is the total flux, $\xi \equiv [(x^2+z^2)/2 + y^2]/\rho_0^2$, and β is a dimensionless parameter describing the self-twist of the bipole. While we use idealized bipoles, it should be noted that recently Hoeksema et al. (2020) have carried out a 3D magnetofrictional simulation of an active region in spherical coordinates using the direct assimilation of magnetogram data. Also, as an alternative to using idealized bipoles in the flux transport model, Yeates (2020) considered the consequences of using the original active region patches for the evolution of the radial field at the photosphere.

To consider how the accuracy and cadence of new bipolar regions affects the results, two data sets of the properties of new bipoles are constructed. One data set is determined from SDO/HMI Carrington rotation synoptic magnetograms that are constructed from data taken during central meridian passage. This bipole data set is described as the "low-cadence" data, as one map per 27 days is used to identify and determine the properties of the bipoles. This corresponds to the cadence that has been used in previous studies (Yeates et al. 2008; Yeates 2014).[3] The second bipole data set is determined from the Advective Flux Transport (AFT) simulations of Upton & Hathaway (2014a, 2014b). The AFT simulations use a combination of data assimilation of SDO/HMI full disk magnetograms, combined with flux transport processes, to simulate the radial magnetic field at the photosphere globally on the Sun. The AFT synoptic magnetograms differ from standard Carrington rotation or daily synoptic maps in a number of ways. For the present study, the most significant differences are that they allow the assimilation of active regions both pre- and post-central meridian and are provided with a one-hour cadence. The bipoles determined from the AFT data are described as the "high-cadence" data set. The low- and high-cadence data sets represent two extremes for data that can be used to identify bipoles. In principle, a third bipole data set could be constructed from SDO/HMI daily synchronic maps that incorporate observational data from $\pm 60°$ of central meridian. These maps are expected to produce bipole properties and numbers in between those found for the low- and high-cadence data sets, but closer to the high-cadence data. Due to this, the present study focuses only on the high- and low-cadence data sets produced from AFT and SDO/HMI Carrington rotation synoptic magnetograms.

[3] These previous studies used NSO/Kitt Peak or SOLIS data, but SDO/HMI data are used here because there was a data gap in SOLIS data from 2014 August to October.

2.2.1. High-cadence Bipole Data Set

To identify the new bipolar active regions from the AFT data, a multi-stage semi-automated process is applied.

1. Over the entire simulation period from 2014 September 1 to 2015 March 30 the absolute value of each AFT map at 12:00 UT is taken, where values less than 20G are set to zero and the map is smoothed through applying a Gaussian filter.
2. Next, a time series of difference maps is computed from the smoothed maps, where the previous map is subtracted from the following one. Successive difference maps are compared and new positive regions (hotspots) covering 15 or more clustered pixels are identified and their longitude and latitude are stored.
3. For each identified hotspot, the evolution of the signed magnetic field from the original untreated AFT data is visually inspected every 6 hr, from 48 hr prior and 120 hr after identification. From this, cases of new emerging flux are identified, where the longitude and latitude are retained for Stage 4. Otherwise, the points are discarded.
4. For each bipole, its properties are then determined from the original 1 hr untreated AFT data. The bipole is followed 48 hr prior to and 120 hr after first identification. At its time of maximum flux, its longitude, latitude, time of emergence, flux, and tilt angle are determined, where once again pixel values less that 20G are set to zero.
5. Over the entire simulation period of 210 days, a total of 197 bipoles are identified.

In carrying out this process, all stages are automated except for stage 3, which is done manually. No specific criteria on the size or flux of the bipoles are made, except in identifying the hot spots in stage two. The present value of a 15-pixel area was selected after testing the reliability of the technique over a two-month subset of the data. Reducing this value further increased significantly the number of visual inspections carried out and rejected, but did not lead to any further bipoles being identified. Increasing it beyond 30 pixels led to some bipoles being missed.

An illustration of a new bipole can be seen in Figure 1, where the identification of the emergence of a new bipole is seen between 2014 September 5–7. In Figures 1(a) and (b), portions of the AFT synoptic magnetograms can be seen on the days of (a) 2014 September 4 and (b) 2014 September 6. From these maps, the emergence of a new bipole at approximately (ϕ, λ) = (195°, −10°) is identified (red dashed box) on September 6. Once identified, the variation of the flux of the bipole both pre- and post-identification is considered (Figure 1(c)). The longitude ($\phi = 192.^{\circ}49$), latitude ($\lambda = -9.^{\circ}01$), half separation ($\rho_0 = 2.^{\circ}02$), flux ($\Phi = 7 \times 10^{21}$ Mx), and tilt angle ($\gamma = 7.^{\circ}58$) are then determined at the time of peak flux. These values are then used to include the bipole in the simulations. In total, over the 210-day simulation period, 197 bipoles are identified using this technique, with a total flux of 2.1×10^{24} Mx. This is the same technique that was used in the eclipse study of Mikic et al. (2018).

For the high-cadence data, as a final stage in verifying the bipole data once all of the bipoles have been identified, a surface flux transport simulation of B_r is run, where each day over the 210-day period the radial field from the simulations is compared to that of the AFT maps. To ensure the accuracy of the radial field, the tilt angle of 7 out of 197 bipoles are varied with a manual correction. This manual correction occurred for cases where the bipoles experienced a significant rotation after the time of peak flux, such that the tilt angle at peak flux was not consistent with that found at later stages of decay. This only occurred for bipoles found within activity complexes where there were multiple rapidly evolving polarities in close

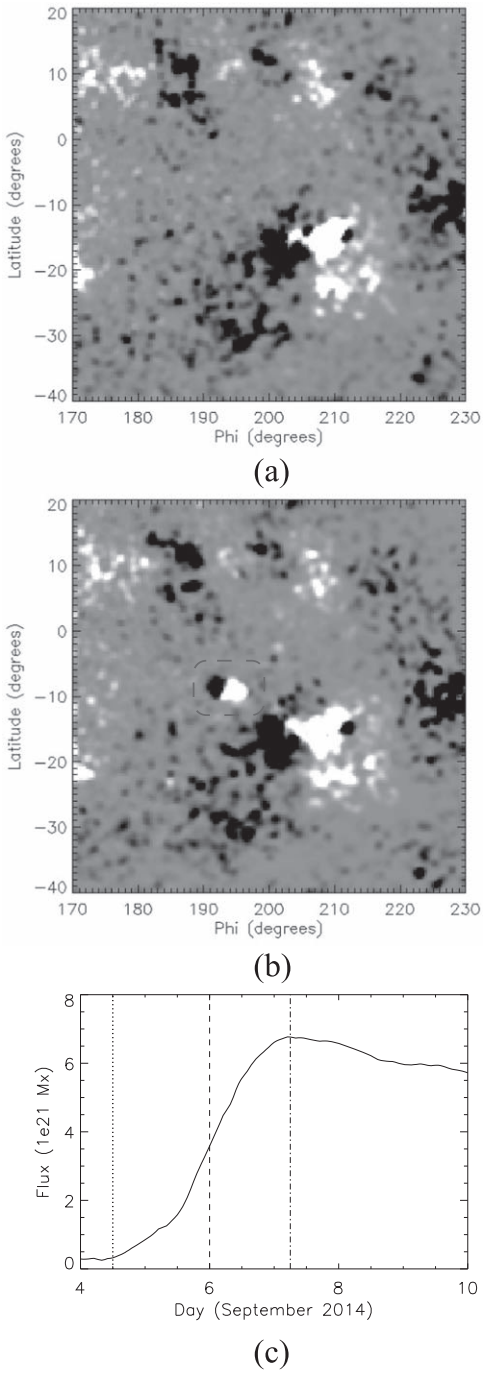

Figure 1. Portions of AFT magnetograms at (a) 12:00UT on 2014 September 4 and (b) 12:00UT on 2014 September 6. In each plot, white/black denotes positive/negative flux, where the values saturate at ±50 G. (c) Graph of flux against day for the new emerging bipole (solid line). The dotted line denotes the time of panel (a), while the dashed line shows the first identification of the new emerging bipole (red dashed box) at the time of panel (b). The dashed–dotted line gives the time of maximum flux where the bipole properties are determined.

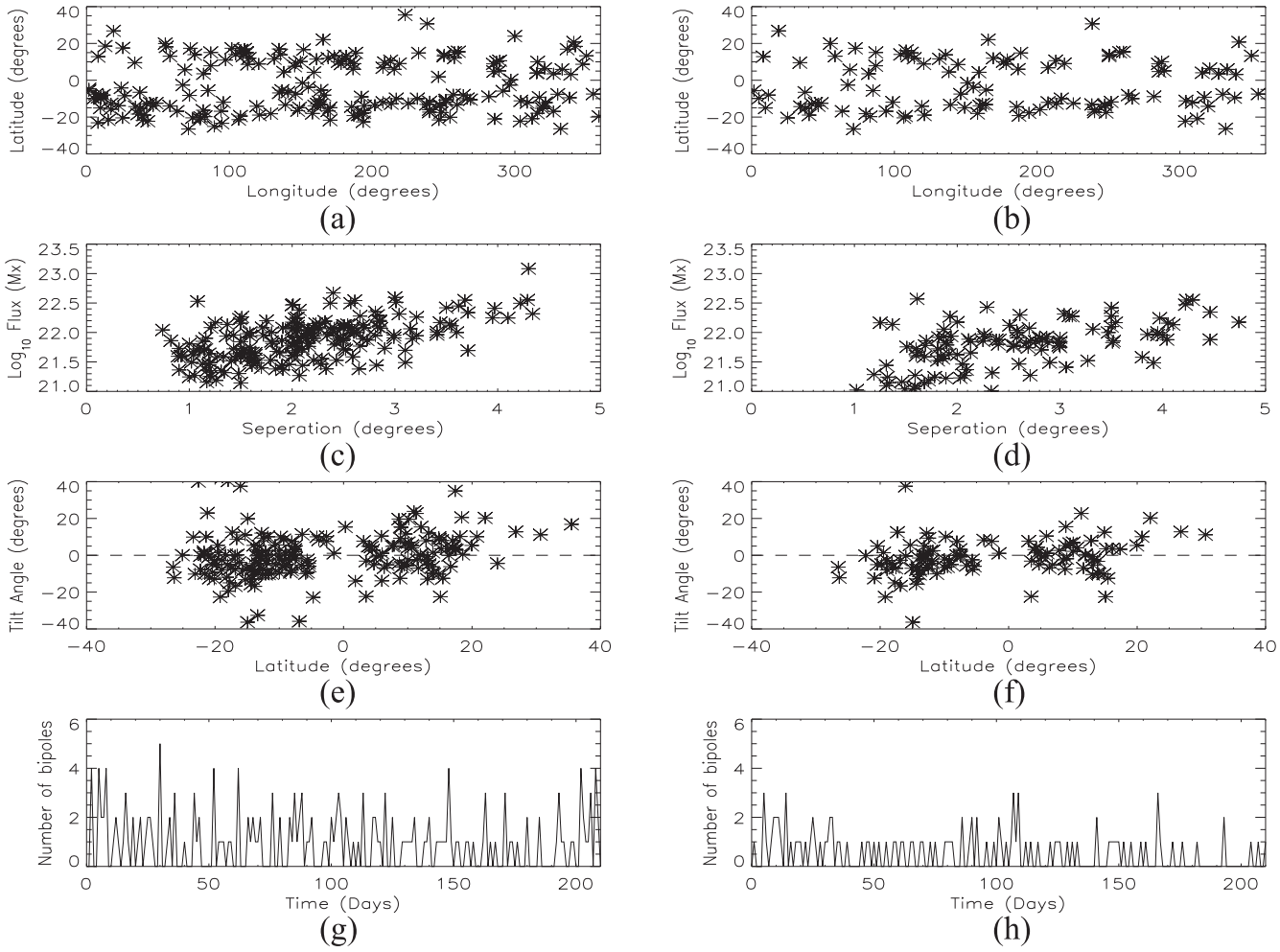

Figure 2. Properties of the new emerging bipoles determined from the high-cadence AFT model (left column) and low-cadence SDO/HMI Carrington rotation maps (right column). Panels (a) and (b) show the emergence latitude against longitude. Panels (c) and (d) show the flux against the bipole half separation, while panels (e) and (f) show the tilt angle versus the latitude of emergence. Finally, panels (g) and (h) show the number of bipoles emerging each day over the 210 days of the simulation.

proximity. During the verification process, no missing bipoles from the semi-automated process were identified.

2.2.2. Low-cadence Bipole Data Set

To determine the bipole properties from the SDO/HMI Carrington rotation maps, a much simpler procedure is applied. Each successive map is compared to the prior one, and the emergence of new bipoles is identified, again through constructing a difference map. Once again, the flux, longitude, latitude, separation, and tilt angle are determined, but now, due to the low-cadence data, the time of emergence is set to be the time of central meridian passage of the bipole. This corresponds to the time the bipole was assimilated into the synoptic map. Because the SDO/HMI Carrington rotation maps only capture bipoles as they pass through central meridian, to be included in the map, the bipoles must emerge before or at central meridian. As a consequence, fewer bipoles are identified over the same simulation period compared to the high-cadence AFT data. The number of bipoles drops to 110 with a total flux of 1.1×10^{24} Mx. For the low-cadence data, the bipole identified in Figure 1 is missed because it emerges post-central meridian.

2.2.3. Comparison of Bipole Data Sets

In Figure 2, the properties of the new emerging bipoles from the high-cadence (left column) and low-cadence (right column) data sets are shown. Figures 2(a) and (b) show graphs of longitude versus latitude. For these plots, there is a clear one-to-one relationship between bipoles in both data sets. However, significantly fewer bipoles are identified when using the low-cadence data.

In Figures 2(c) and (d), graphs of flux versus bipole half separation are shown. In both data sets, a wide range of fluxes and sizes occur, where fluxes range from 1 to 100×10^{21} Mx and half separations from 1° to 5°. For these graphs, there is no one-to-one relationship between the data sets. Upon directly comparing the flux values for the same bipoles identified in both data sets, the bipoles in the low-cadence data set have lower values, as their flux is determined at central meridian passage rather than at their peak value. The low-cadence bipoles may have either larger or smaller half separations compared to the same bipole identified in the high-cadence data. Larger half separations arise for bipoles that are decaying during central meridian passage, while lower separations arise for those still in the process of emerging as they pass through central meridian.

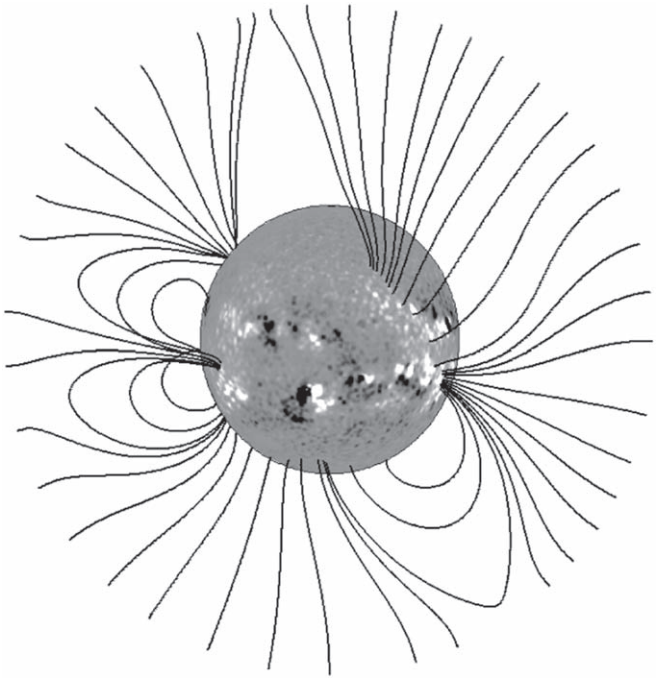

Figure 3. The PFSS initial condition used for all of the simulations determined from the AFT map at 12 noon on 2014 September 1. The grayscale image shows the radial field at the photosphere, where white/black represents positive/negative flux, where the values saturate at ±50 G. The black lines denote the field lines extending up to the source surface at $2.5R_{\odot}$.

In Figures 2(e) and (f), the tilt angle of the bipoles is given as a function of latitude of emergence. Positive/negative values denote bipoles that satisfy Joy's law in the northern/southern hemispheres, respectively. It can be seen that, for both data sets, there is a wide scatter; however, the bipoles follow Joy's law. As the tilt angle evolves relatively slowly during disk transit, where a bipole exits on both data sets, there is a one-to-one relationship. Finally, Figures 2(g) and (h) show the number of bipoles emerging each day throughout the 210 days of the simulation. For both the high- and low-cadence data sets, bipoles emerge throughout the entire period of the simulation without any significant clustering of the missing bipoles in the low-cadence data set. From Figure 2(g), it is clear that a higher number of bipoles emerge throughout the simulation for the high-cadence data set.

The observationally derived properties of the bipoles shown in Figure 2, along with the analytical form of the bipoles given in Section 2.2, are used to specify the source function for the emergence of new magnetic bipoles. The bipoles are emerged by the process described in Mackay & van Ballegooijen (2001) and Yeates et al. (2008).

2.3. Initial Condition

All simulations presented in Section 3 have the same initial condition even when the bipoles are determined from different sources. Because we use the same initial condition, we know that any subsequent differences are solely a consequence of the cadence and properties of the emerging bipoles determined from the high- or low-cadence data sets or the terms applied in the solar corona. The initial condition is chosen to be a Potential Field Source Surface (PFSS) model with the source surface at $2.5R_{\odot}$ (Schatten et al. 1969; Altschuler & Newkirk 1969; Virtanen & Mursula 2016; Badman et al. 2020). It is constructed using the AFT map from 1200 UT on 2014 September 1 at 1° resolution and can be seen in Figure 3. As it is unlikely that the solar corona was in a potential state at this time, the first 54 days (8 weeks) of the simulation are used as a ramp-up phase (Yeates et al. 2008). During this period, the initial potential nature of the coronal field is removed through a combination of surface motions and magnetic flux emergence, and the corona develops into a self-consistent non-potential state.

3. Simulation Results

For the comparison between the observations and simulations, five separate parameters are varied. These include the bipole data set, the bipole twist, the coefficients of hyperdiffusion or ohmic diffusion, and finally the vorticity in the SAHC model. As many of these quantities may take a range of values, there are a large number of combinations that can be considered. Based on previous studies, 28 separate simulations are run, where the properties of the simulations are given in Table 1. These 28 simulations are designed to cover a range of possible scenarios along with comparing parameter values used in previous studies. While the simulations are numbered 1–14, each is run twice, once using the high-cadence bipole data from AFT and once using the low-cadence SDO/HMI data. All simulations using the high-cadence data produce an identical distribution of the radial magnetic field at the solar photosphere. Correspondingly, all simulations using the low-cadence data also produce an identical distribution of the radial magnetic field, but over time, this diverges from the high-cadence case. In addition to the simulations outlined in Table 1, an additional simulation that uses an inductive electric field (Mackay et al. 2011; Weinzierl et al. 2016) to drive the evolution of the radial magnetic field at the photosphere is carried out. This solution was computed directly from the AFT magnetograms with a cadence of one day. Results from this run are not shown, as when using this alternative technique, the coronal field remained close to potential.

3.1. Radial Field on 2015 September 20

Figure 4 presents a comparison of the radial magnetic field from the simulations using both the high- and low-cadence bipole data sets with the observed AFT map at 1200 UT on 2015 September 20. In each panel, white/black represent positive/negative flux, where the values saturate at ±50 G, and the vertical dashed line indicates the Carrington longitude that lies at central meridian. Figure 4(a) presents the AFT map, where it has been smoothed using a Gaussian filter such that the resolution of the displayed image is consistent with the resolution of the simulations. Figure 4(b) presents the results of the simulation using the high-cadence bipoles determined from AFT, while Figure 4(c) shows the low-cadence simulation. Upon comparing both simulations with the observationally derived AFT map, it can be seen that there is general agreement even though they do not match on a pixel-by-pixel basis. However, it is clear that the simulation using the high-cadence bipole data produces a much better agreement compared to the simulation using the low-cadence bipoles. Key locations where differences arise are given by the labels 1–5 in Figure 4(a), where the low-cadence simulation has failed to reproduce the complexity found in the AFT data, which are derived from observations. This complexity has, however, been

Table 1
List of 28 Simulations That Are Compared on 2015 March 20

Run No	Name	Bipole Origin	Bipole Twist	HD (km^4s^{-1})	ohmic (km^2s^{-1})	Vorticity (s^{-1})
1	IdealA0/IdealH0	AFT/HMI	0.0	0.0	0.0	0.0
2	IdealA2/IdealA2	AFT/HMI	0.2	0.0	0.0	0.0
3	IdealA4/IdealH4	AFT/HMI	0.4	0.0	0.0	0.0
4	IdealA6/IdealH6	AFT/HMI	0.6	0.0	0.0	0.0
5	HDA0/HDH0	AFT/HMI	0.0	1e11	0.0	0.0
6	HDA2/HDH2	AFT/HMI	0.2	1e11	0.0	0.0
7	HDA4/HDH4	AFT/HMI	0.4	1e11	0.0	0.0
8	HDA6/HDH6	AFT/HMI	0.6	1e11	0.0	0.0
9	OhmA0/OhmH0	AFT/HMI	0.0	0.0	60.0	0.0
10	OhmA2/OhmH2	AFT/HMI	0.2	0.0	60.0	0.0
11	OhmA4/OhmH4	AFT/HMI	0.4	0.0	60.0	0.0
12	OhmA6/OhmH6	AFT/HMI	0.6	0.0	60.0	0.0
13	SAHCA1/SAHCH1	AFT/HMI	0.0	0.0	0.0	1e-6
14	SAHCA5/SAHCH5	AFT/HMI	0.0	0.0	0.0	5e-6

reproduced using the high-cadence bipole data. The main reason for these differences is that bipoles are emerging either after central meridian passage, such as occurs for locations 2–5, or where they have not yet rotated through central meridian and as such are not yet included (location 1). Such missing features can have a significant effect on the structure of the corona and on the comparison with coronal observations on a given day. In particular, locations 1–3 all lie on the visible disk, while location 4 is at the limb. The consequences of this for reproducing either the on-disk features such as solar filaments or off-limb structures such as coronal loops will be considered in Sections 3.3 and 3.4.

3.2. Global Parameters

Figure 5 shows the variation of the surface flux (Equation (10)) over the 210 days of the simulation for the high-cadence (solid line) and low-cadence (dashed line) simulations. In each plot, the triangles denote the surface flux calculated from the AFT data (blue) and HMI Carrington rotation maps (red). The flux computed from the HMI Carrington rotation maps is computed once every 27 days, where the horizontal red line denotes the time period of the map. For the AFT data, the flux is average over a 10-day period given by the horizontal blue line. Each of the simulations reproduces the characteristic variations of the surface flux found in the observations.

Both simulations start with the same flux value and exhibit a similar behavior. Over the first 100 days, there is an overall increase of flux, followed by a general decrease until the day of the eclipse (day 200, vertical dotted line). The injection of the bipoles can be seen in both curves as the sharp rise in flux values. The most prominent of these occurs around day 50, where there is the emergence of a large activity complex in the southern hemisphere that remains for a number of rotations. While both simulations show a similar behavior, the high-cadence bipole data simulation produces significantly higher flux values, due to the larger number of injected bipoles. Such a difference between the simulations occurs straight after the start, where on day 5, there is a sharp increase in flux in the high-cadence simulation that is missing from the low-cadence one. This departure is then maintained and enhanced due to the continuous nature of the simulations.

Figure 6 presents results for the total magnetic energy (Equation (11)) and total volume-integrated electric current (Equation (12)) for the simulations listed in Table 1. Figures 6(a) and (b) show the time series variation of these quantities for a subset of the simulations, where the bipole twist parameter is set to zero ($\beta = 0$). Results for both the high-cadence bipole data set (solid lines) and low-cadence bipole data set (dashed lines) are shown. The black lines represent ideal simulations (IdealA0/IdealH0), green lines are for simulations with ohmic Diffusion (OhmA0/OhmH0), blue lines are for hyperdiffusion (HDA0/HDH0), and red lines are for SAHC with a vorticity of 1×10^{-6} s^{-1} (SAHCA1/SAHCH1).

$$\Phi_s(t) = R_\odot^2 \int_S |B_r(R_\odot, \theta, \phi, t)| d\Omega \tag{10}$$

$$E_{\rm mag}(t) = \frac{1}{8\pi} \int_V B^2(r, \theta, \phi, t) d\tau \tag{11}$$

$$J_v(t) = \int_V |J(r, \theta, \phi, t)| d\tau \tag{12}$$

From Figure 6(a), it is clear that the volume-integrated magnetic energy closely follows the variation of the surface flux. While each simulation shows the same general trend, the exact values obtained very much depend on the cadence of the bipole data and the coronal physics included. Simulations using the high-cadence bipole data have a systematically higher energy compared to the low-cadence simulations. In addition, the ideal simulations (black and red lines) have a systematically higher energy than the corresponding nonideal ones (green and blue lines). It is also interesting to note that, for the nonideal simulations, those using hyperdiffusion (blue lines) have a slightly lower energy compared to ohmic diffusion (green lines). Overall, the simulations with SAHC have the highest energy, as they have an extra source of energy injection. Similar results and ordering of the values are found when the twist parameter of the bipoles is varied. Increasing this parameter leads to an overall increase of energy compared to the values found in Figure 6(a). From considering the difference between the curves, it is clear that the cadence of the bipoles has a greater effect on the stored magnetic energy compared to that of the coronal physics.

Figure 6(b) presents a similar graph, but now for the volume-integrated electric current (Equation (12)), where the colors and

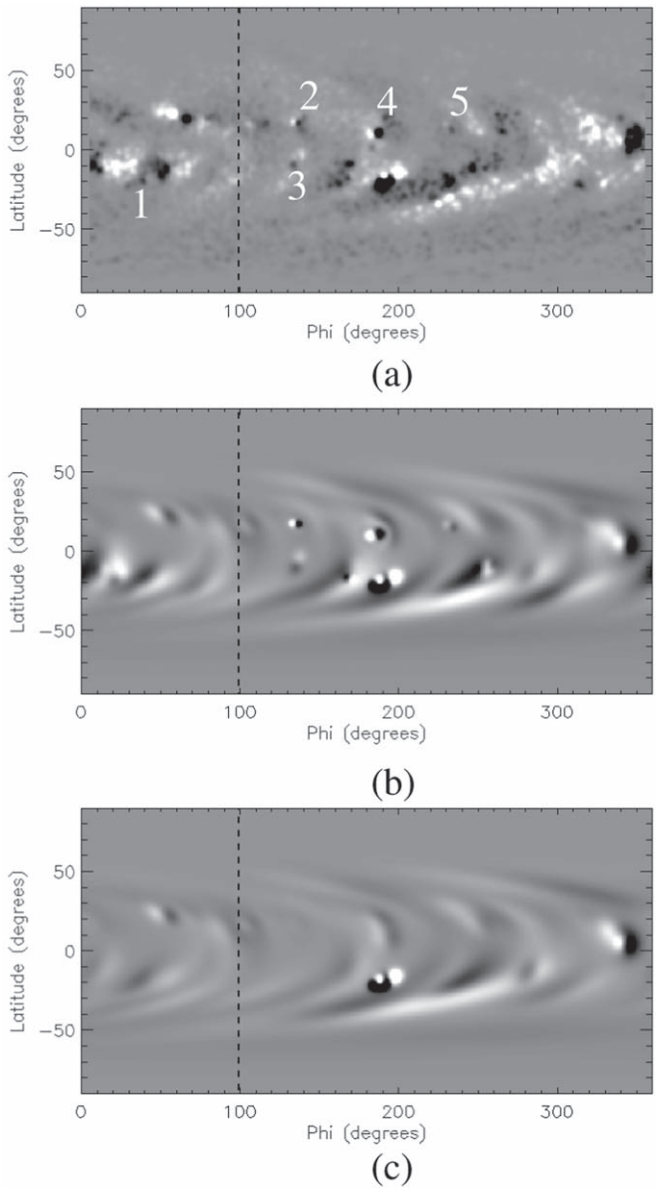

Figure 4. Comparison of (a) the AFT map derived from observations at 12 noon on 2015 March 20 with (b) the flux transport simulation using bipoles derived from the daily AFT maps and (c) the flux transport simulation using bipoles derived from HMI Carrington rotation maps. Panels (b) and (c) are shown on the same date and time as panel (a). In each panel, the radial field at the photosphere is shown, where white/black represent positive/negative flux, where the values saturate at ±50 G. The image in panel (a) has been smoothed with a Gaussian filter to match the resolution of the simulations. In panel (a), key bipoles are identified with the numbers 1–5. In each panel, the dashed lines denote the longitude at central meridian on the 2015 March 20 at 12 noon.

line styles are the same as in Figure 6(a). Each of the simulations follows a similar behavior. Over the first 100 days, the volume-integrated electric current increases from zero to reach a near-steady state. This indicates that a balance between injection and loss has been achieved. A similar pattern of the ordering of the simulations occurs, where the simulation with SAHC contains the largest electric current and those with hyperdiffusion the lowest. The difference between the highest and lowest curves is around a factor of two. In contrast to the volume-integrated magnetic energy, the cadence of the bipoles used to drive the simulation has a much smaller effect compared to the coronal physics. Also, for the vast majority

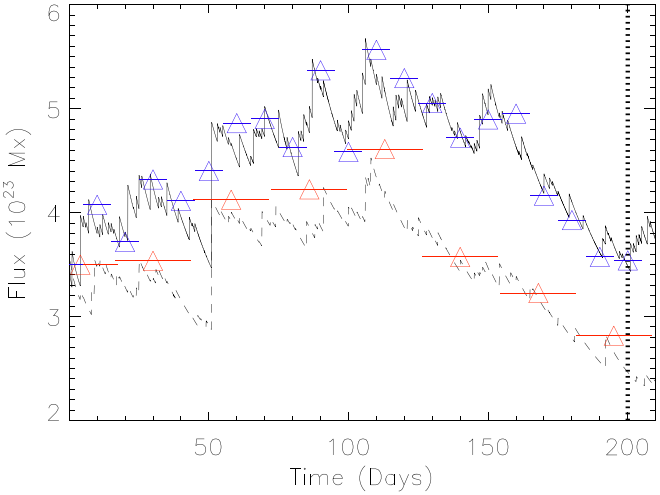

Figure 5. Variation of the photospheric flux over the 210 days of the simulation from 2014 September 1 to 2015 March 30. The solid line denotes the simulation using bipoles determined from the AFT magnetograms, while the dashed line is for bipoles determined from HMI Carrington rotation synoptic maps. The triangles denote the surface flux computed from both the AFT magnetograms (blue) and HMI Carrington rotation maps (red). The horizontal red and blue lines denote the time period over which the flux is calculated in each data set. The vertical dotted line gives the time of the eclipse on 2015 March 20.

of the bipoles, there is no significant increase in the volume electric current as the bipoles are emerging. This is expected, as the bipoles are inserted in a non-sheared state. The only exception to this is the emergence of the activity complex in the southern hemisphere on day 50.[4]

In Figures 6(c) and (d), the results from all of the simulations can be seen on day 200, the date of the eclipse for both the magnetic energy and volume-integrated electric current, respectively. On each graph, the results are collated depending on the coronal physics included (ideal, ohmic dissipation, hyperdiffusion, and SAHC), along with the twist parameter used for the bipoles (black $\beta = 0$, blue $\beta = 0.2$, green $\beta = 0.4$, and red $\beta = 0.6$). The simulations using the high-cadence bipole data are given by the diamonds, while those using the low-cadence data are given by stars. For the simulations involving SAHC, two values of vorticity are used: 1×10^{-6} s^{-1} (light blue) and 5×10^{-6} s^{-1} (yellow). In Figure 6(c), the solid and dashed horizontal lines denote the energy of a PFSS model that satisfies the same normal field component at the photosphere $r = R_{\odot}$. While this line provides an approximate lower bound for the magnetic energy, care must be taken if using this to calculate the free magnetic energy, as only the normal field component at the photosphere ($r = R_{\odot}$) is matched. A limited number of calculations were carried out to determine the potential field matching the radial field at both $r = R_{\odot}$ and $r = 2.5R_{\odot}$ through relaxing the non-potential fields back to potential. While this process was computationally extremely time consuming, values for the total magnetic energy were within 5% of the values found for the PFSS model. We therefore only present the PFSS value, as it is less complex than presenting 24 different values all with negligible differences.

From Figure 6(c), it is clear that all of the high-cadence simulations have much higher energy than the low-cadence ones on the date of the eclipse. The low-cadence simulations

[4] Due to the log scale, care must be taken in comparing jumps in separate curves.

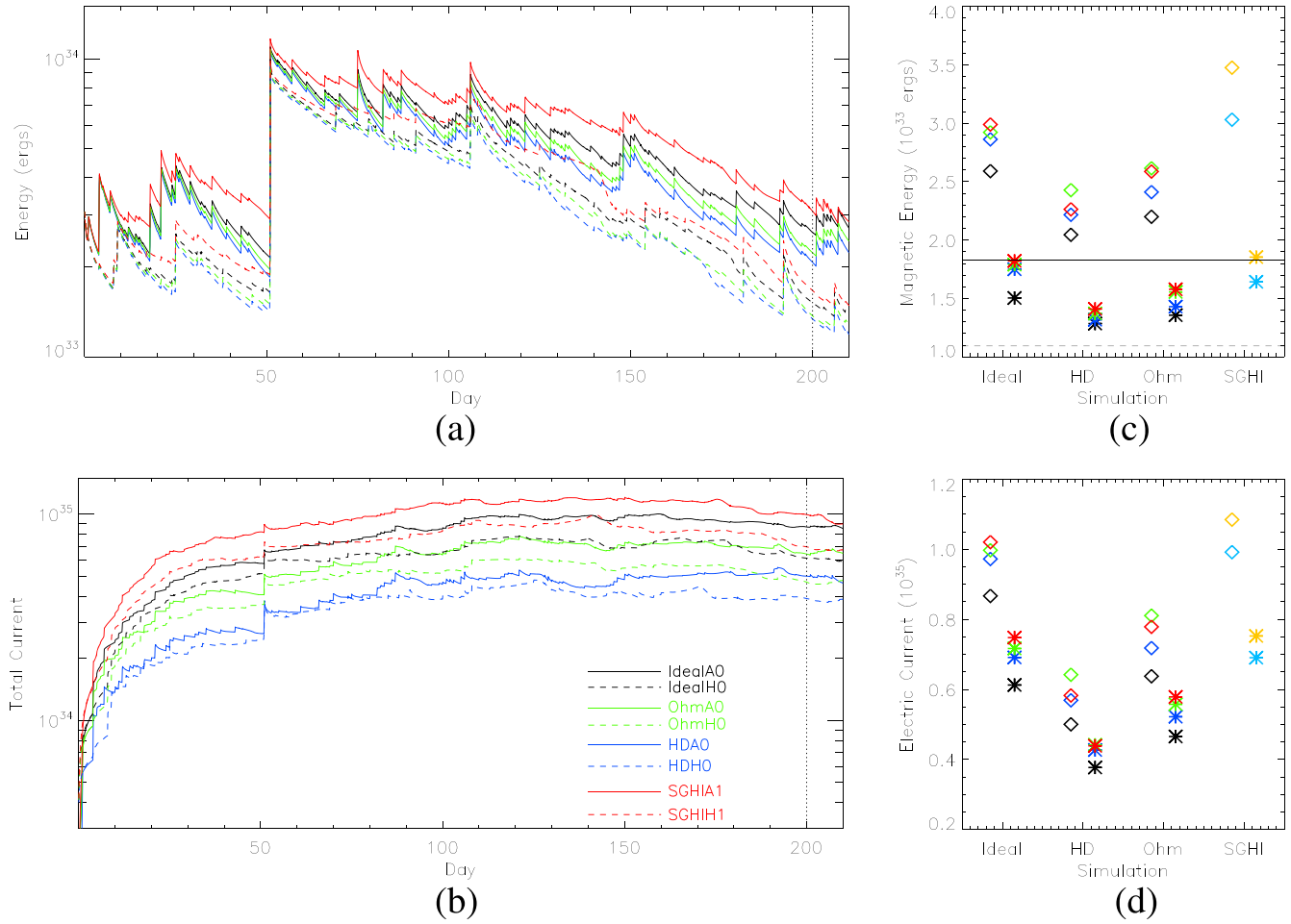

Figure 6. Graphs of (a) and (c) magnetic energy and (b) and (d) volume-integrated electric current. Graphs (a) and (b) show the magnetic energy and volume-integrated electric current as a function of time for the simulations using the bipoles determined from the high-cadence (AFT maps, solid lines) and low-cadence (HMI Carrington maps, dashed lines). The legend in graph (b) describes the line styles and colors, where in each case black denotes the ideal simulations (IdealA0 and IdealH0), green the simulations with ohmic dissipation (OhmA0 and OhmH0), blue the simulations with Hyper Diffusion (HDA0 and HDH0), and red simulations with Statistically Averaged Helicity Condensation (SAHCA1 and SAHCH1). For all of the simulations, the bipoles are inserted with zero twist. Graphs (c) and (d) show the magnetic energy and volume electric current on 2015 March 20 for all simulations. The diamonds denote the simulations using bipoles determined from the AFT data, and the stars the simulations using bipoles determined from HMI Carrington rotation synoptic maps. Black has the bipole twist parameter $\beta = 0$, blue $\beta = 0.2$, green $\beta = 0.4$, and red $\beta = 0.6$. The light blue and yellow colors denote supergranular vorticity of 1×10^{-6} s^{-1} (light blue) and 5×10^{-6} s^{-1} (yellow).

tend to have a total non-potential energy less than that of the energy of the PFSS model determined from the high-cadence simulation. In general, for all simulations, as the bipole twist parameter or SAHC vorticity rate increases, higher energies are found. For some simulations, this is not the case; however, this arises when flux ropes storing a significant amount of energy are ejected from the simulation (Bhowmik & Yeates 2021). As the bipole twist increases, this occurs more frequently in the simulations. Overall, the simulations using the high-cadence bipoles contain 60%–80% more energy than those from the low-cadence data set on the day of the eclipse. Figure 6(d) presents the same results for the volume-integrated electric current, where the results and color coding are the same as those used for Figure 6(c). As expected, the simulations using the high-cadence bipole data have a higher electric current, however this time the coronal physics plays a stronger role than that found for the magnetic energy.

From the above graphs, it is clear that a wide range of energies and volume-integrated electric currents can be found, depending on the cadence of the bipole data and the coronal physics. It is also clear that the amount of energy stored in the corona depends mostly on the complexity of the photospheric and coronal field. This arises due to two main reasons. First, more complex fields arise due to higher numbers of new emerging bipoles in the simulation, which naturally increases the energy. Second, even though all of the simulations have the same horizontal velocity at the photosphere, once emerged, each bipole leads to an increased Poynting flux injection, due to the increased normal and horizontal field components. Subsequently, the more complex the field at the photosphere, the more energy that can be injected, due to horizontal surface motions as the bipoles decay over extended periods of time. While the energy stored does depend on the coronal physics, this has less of an effect. In contrast, the corona physics has a more significant effect on the volume-integrated current. Overall, simulations using hyperdiffusion lead to smaller magnetic energies and weaker electric currents compared to the other ideal and nonideal simulations. This will have a significant impact on the structure and connectivity of the coronal field, which is investigated next.

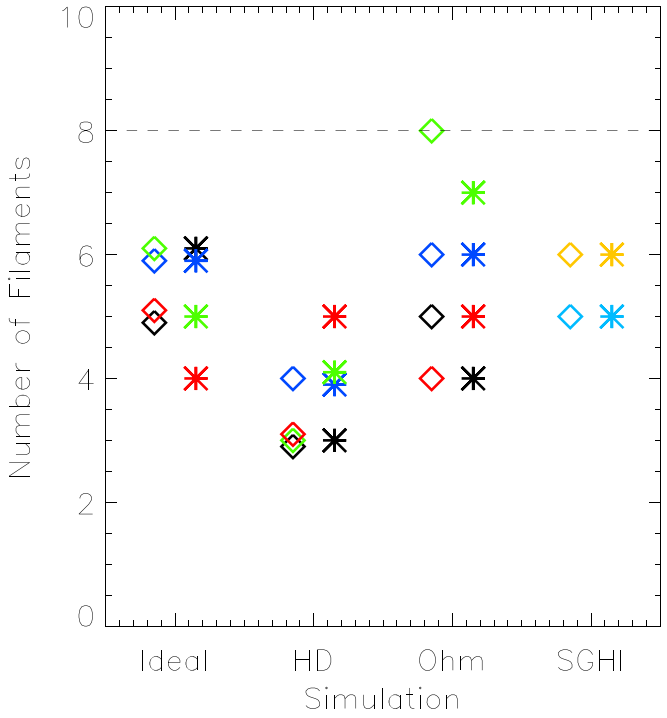

Figure 7. Scatter plot of the number of filament locations reproduced by the simulations, based on the coronal physics included. The diamonds denote the simulations using bipoles determined from the AFT simulations, and the stars the simulations using bipoles determined from HMI Carrington rotation synoptic maps. Black color denotes a bipole twist parameter $\beta = 0$, blue $\beta = 0.2$, green $\beta = 0.4$, and red $\beta = 0.6$. The light blue and yellow colors denote supergranular helicity injection at respective rates of 1×10^{-6} s^{-1} (light blue) and 5×10^{-6} s^{-1} (yellow). The horizontal dashed line denotes the number of observed filaments.

3.3. Comparison with Solar Filaments

Solar filaments (Labrosse et al. 2010; Mackay et al. 2010) and their birth grounds, filament channels (Gaizauskas 1998), are key indicators of the location of non-potential fields and the storage of free magnetic energy in the solar corona. The generation, transport, and storage of this energy is important for understanding global evolution processes on the Sun and explaining eruptions outside of active regions (Yardley et al. 2021). To consider how well each of the simulations given in Table 1 reproduces the locations of solar filaments, we now consider whether the simulations produce either a strongly sheared arcade (Antiochos, Dahlburg & Klimchuk 1994; DeVore & Antiochos 2000) or a magnetic flux rope (Kuperus & Raadu 1974; Rust & Kumar 1994; Aulanier & Demoulin 1998; Gibson & Fan 2006) at the observed filament locations on the day of the eclipse. The results of how well each of the simulations perform are given in Figure 7, while illustrations of a characteristic sample of the results are given in Figure 8.

Figure 8(a) shows a full-disk Hα image taken by Big Bear Solar Observatory (BBSO) at 18:54 UT on 2015 March 20. This is on the same day as the solar eclipse, but at a later time. A total of eight distinct solar filaments can be seen across the visible solar disk. Each outlines a strongly sheared magnetic field that extends from the solar chromosphere and into the solar corona. Of the eight identified filaments and filament channels, four (numbers 1–4) are large structures and three (numbers 5, 7, and 8) are small structures. Number 6 only exhibits weak absorbing material in Hα. However, for this filament, the presence of a circular filament channel is clearly seen in UV images. Filament number 3 has an extension both on the solar disk and at the east solar limb.

In Figure 7, the symbols and color coding are the same as in Figure 6. The vertical axis gives the number of sheared non-potential magnetic fields or flux ropes produced by each of the simulations at the observed location of the solar filaments. The target number of eight is given by the dashed line. To identify sheared non-potential fields or flux ropes, field lines are plotted above the respective polarity inversion lines starting at a height of 10,000 km. The identification of a flux rope from these field lines is straightforward; however, the identification of strongly sheared arcades is more subjective. For the present study, a sheared arcade is counted as producing the correct non-potential field if it makes an angle of less than 20° to the polarity inversion line along the observed length of the filament. This value is chosen based on results found for filament observations using the Hanle effect (Bommier et al. 1994). To consider the robustness of this classification, the angle has been varied by $\pm 10°$; however, doing so does not change the results.

From Figure 7, it is apparent that both the applied coronal physics and helicity injection mechanisms have an effect on the production of sheared non-potential fields at the location of the filaments. Only one simulation, the high-cadence simulation with ohmic dissipation and a bipole self-twist of $\beta = 0.4$, reproduces all of the filaments. This result can be seen in Figure 8(b), where a selection of field lines are shown. In contrast to previous results, simulations using the low-cadence bipole data do not produce results significantly different from those using the high-cadence data. The most notable difference is that, when using the low-cadence data, the circular PIL at the location of filament 6 is not produced. As a consequence, these simulations cannot capture this filament. An illustration of field lines in a low-cadence simulation can be seen in Figure 8(c), where the same simulation parameters are used as in Figure 8(b). From considering Figure 7 and the field lines produced from each simulation, it is clear that the cadence of the bipole data has little effect on the accuracy of the non-potential structures at the locations of the solar filaments, as long as the emerging bipoles produce the correct path of the polarity inversion line. This explains why Yeates et al. (2008) were able to accurately reproduce the chirality of filaments during their study, even though only low-cadence Kitt Peak Carrington rotation synoptic maps were used. Therefore, within the context of producing filaments or filament channels, any variation in the properties of the non-potential fields along the polarity inversion lines must be due to the coronal physics and the range and variety of helicity injection mechanisms applied.

In all of the simulations, increasing the bipole twist parameter from $\beta = 0$ to 0.6 does not guarantee a better agreement in reproducing the observed locations of the filaments at this fixed point in time. The reason is that increasing this rate reduces the time to form a sheared field or flux rope along the PIL. However, once formed, the flux rope may then erupt, removing the shear and leaving a weakly sheared arcade behind (Pagano et al. 2013a, 2013b, 2018). Successfully reproducing the filaments is a balance between injection, localization along the PIL, and subsequent removal by loss of equilibrium. For the majority of the simulations that include bipole twist, this is best captured using β in the range 0.2–0.4 (blue and green symbols), but exceptions to this exist.

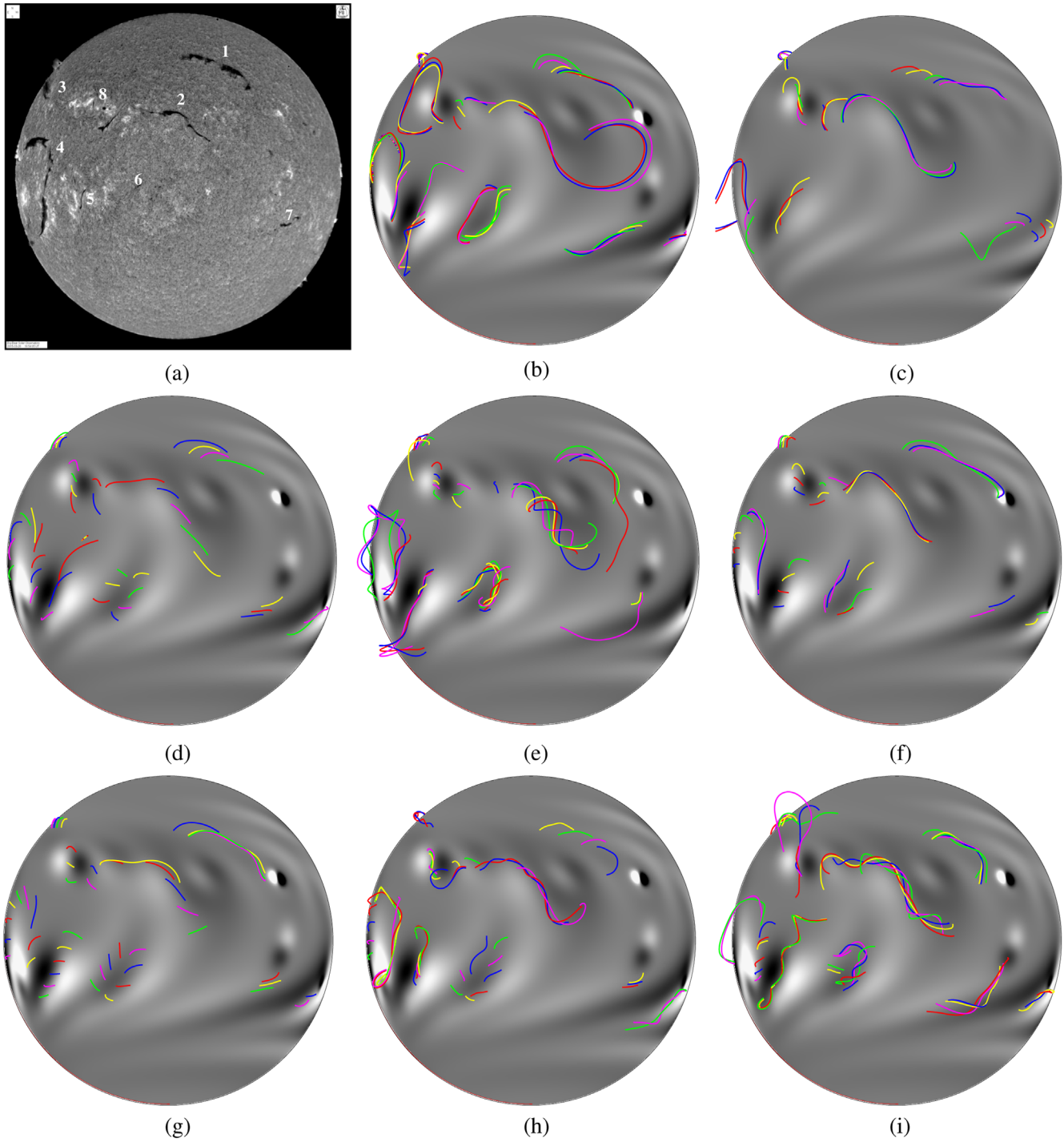

Figure 8. Comparison of the field lines at the locations of the observed filaments. (a) Hα from BBSO taken on 2015 March 20 at 1845UT, where eight filaments are labeled. Panels (b)–(i) present the results for runs. (b) OhmA4: eight filaments, (c) OhmH4: seven filaments, (d) HDA4: three filaments, (e) IdealA4: six filaments, (f) OhmA0: five filaments, (g) HDA0: three filaments, (h) IdealA0: five filaments, and (i) SHGIA1, five filaments. In each of panels (b)–(i), white and back respectively represent positive and negative flux, where the values saturate at ± 20 G. All of the simulation results are derived from using the AFT high-cadence bipole data, except for panel (c), which uses the lower-cadence HMI bipole data.

Figure 8(f) shows the resulting field lines when the equivalent simulation to Figure 8(b) is carried out, but now with $\beta = 0.0$. As a consequence, less sheared structures are produced.

The ideal simulations produce results very similar to those of the simulations with ohmic dissipation as the bipole twist parameter is varied. An illustration of the results produced using ideal simulations can be seen in Figures 8(e) and (h), where the respective bipole twist parameters are $\beta = 0.4$ and 0.0. The main difference between the ideal and ohmic dissipation simulations is that the ideal simulations tend to produce much more strongly twisted flux ropes (compare filament 2 in Figures 8(b) and (e)). In both sets of simulations, the optimal value for the bipole twist parameter is $\beta = 0.2 - 0.4$, where higher or lower values produce worse results.

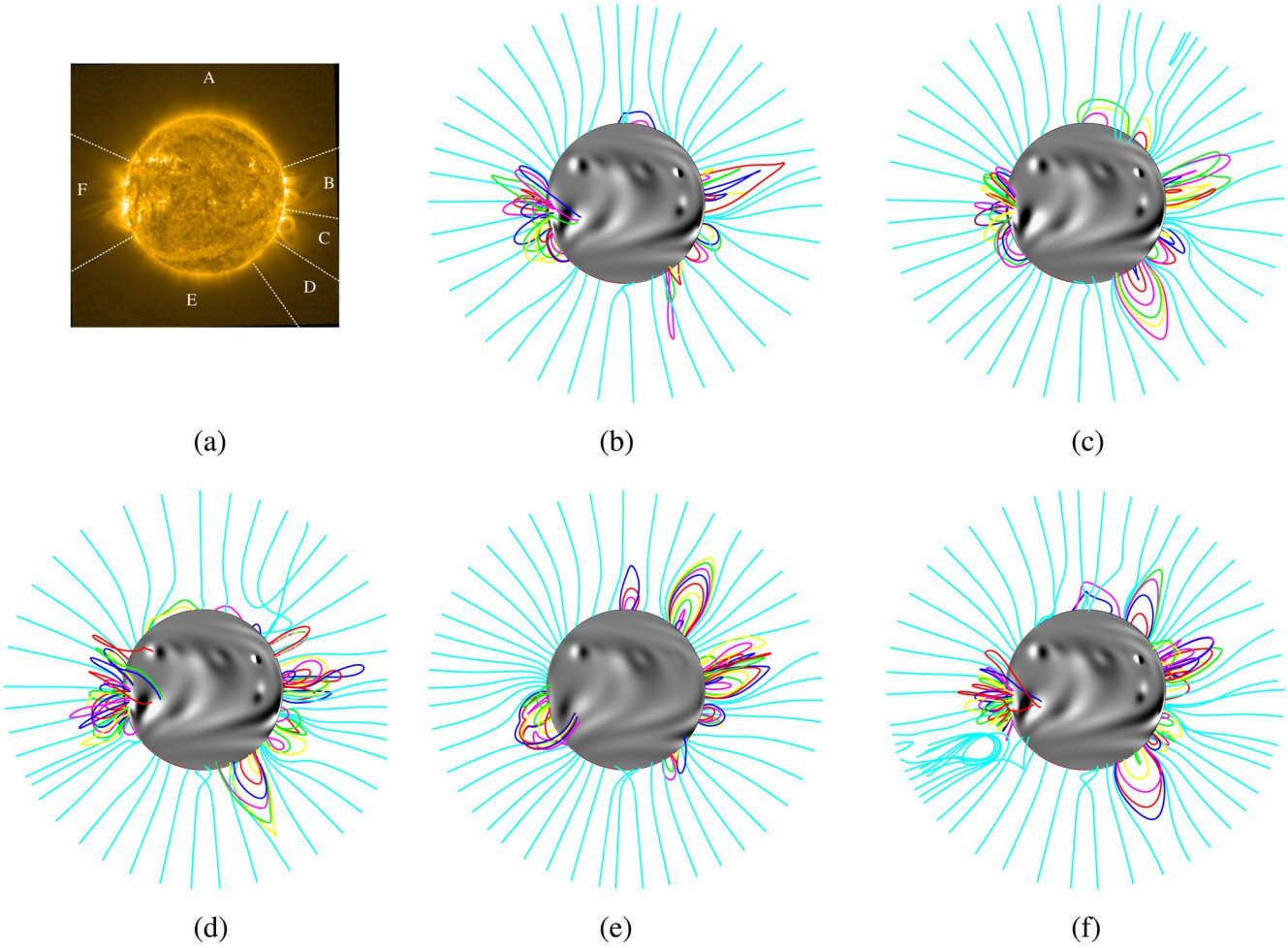

Figure 9. (a) PROBA2/SWAP 174 Å image taken on the 2015 March 20 at 12:00UT, showing the large-scale off-limb structure of the solar corona. The off-limb structures have been divided into six regions where regions A and E denote faint open fields, while regions B, C, D, and F contain a mixture of bright closed corona loops in addition to faint open fields. Panels (b)–(f) show the results for the plane-of-sky magnetic fields for (b) HDA2, (c) OhmA2, (d) IdealA2, (e) HDH2, and (f) SAHCA1. For each of panels (b)–(f), positive/negative flux is given by white/black, where the field values saturate at ±20 G and the colored lines are the field lines.

Overall, the worst agreement with the filament observations occurs when hyperdiffusion is included where the least number of strongly sheared arcades or flux ropes are formed. Figures 8(d) and (g) show characteristic results when the bipole twist parameter is $\beta = 0.4$ or 0.0, respectively. Even with the inclusion of bipole twist, hyperdiffusion leads to mostly weakly skewed arcades. This may seem counter-intuitive, as the timescale for hyperdiffusion to act is typically much longer than ohmic diffusion, which does form strongly sheared arcades and flux ropes. However, the hyperdiffusion timescale is related to the timescale for the field to relax to a linear-force free state. While this is not achieved, due to the continual evolution of the surface field, hyperdiffusion succeeds in smoothing out gradients in alpha and quickly removes strong electric currents from around PILs. This current is then redistributed more uniformly throughout the corona. As a consequence, phenomena such as filaments and filament channels, which are known to be localized regions of strong shear and electric current, are not well-reproduced.

When SAHC is used as an additional helicity injection mechanism, the best agreement with the observations is found for a vorticity of 1×10^{-6} s^{-1}. The corresponding field lines can be seen in Figure 8(i). It is interesting to note that, even though this simulation is ideal, the SAHC mechanism produces thinner and more localized flux rope structures compared other ideal simulations (Figure 8(e)). When the vorticity is increased to 5×10^{-6} s^{-1} similar thin flux ropes form but at a much faster rate. These flux ropes then erupted prior to the observations, leaving behind weakly sheared arcades that do not match the observations on this given date.

3.4. Comparison with Limb Observations

For the next comparison, we will consider how well each of the simulations reproduces off-limb structures observed in PROBA2/SWAP. While the comparison here focuses solely on the date of the eclipse, the paper of Meyer et al. (2020) compares a single simulation, OhmA4 in Table 1, with PROBA2/SWAP data over the entire simulation period of 210 days. Figure 9(a) shows a PROBA2/SWAP 174 Å image taken at 12:00 UT on 2015 March 20, where a variety of off-limb structures can be seen. These off-limb structures have been divided into zones A–F. Zones A and E denote mainly faint open field regions, while B, C, and F exhibit a mixture of low-lying bright closed coronal loops along with fainter open field lines. Finally, in zone D, a very faint large-scale closed arcade structure exits. While zone A is classified as open, near its boundary with zone B, there is some indication of low-lying closed structures, but the features are very weak. Field

extrapolations from the simulations can be seen in Figure 9(b)–(f), where a mixture of open (cyan colored) and closed field lines are plotted. In selecting the starting points for the fields lines, only points in the plane of the limb are used for both the open and closed structures. While the starting points are in the plane of the limb, subsequent tracing of the field lines may take them out of this plane. This is particularly true for the lower-lying closed field lines. All open field lines have a starting point close to the outer boundary at $2.5R_{\odot}$. Upon comparing all 28 runs, it is found that there is significantly less variability in the limb structures compared to phenomena used for other comparisons. In particular, varying the bipole twist parameter has little effect. Due to this, results in Figure 9(b)–(e) are only shown for the cases with $\beta = 0.2$.

From Figures 9(b)–(f), it can be seen that all of the simulations reproduce the open field regions found around the poles in zones A and E. This is not surprising, as each simulation has only run for 200 days, where the timescale for meridional flow to advect flux from the equator to the poles is 2–3 yr. As a consequence, the majority of the flux in the polar zones is due to that found in the initial condition taken from the observations. While the southern hemisphere is completely open in all of the simulations, in the northern hemisphere there is a small amount of closed flux. In the high-cadence bipole data simulations using hyperdiffusion, ohmic diffusion or ideal coronal physics/processes (Figure 9(b)–(d), respectively), this closed field exists only in the low corona. However, for the cases where hyperdiffusion is combined with the low-cadence bipole data (Figure 9(e)) or high-cadence data are combined with SAHC (Figure 9(f)), large arcade structures are found around a position angle of 330 degrees.[5] From Figure 9(a), there is only limited evidence of such large-scale closed structures at this location.

All of the simulations reproduce the low-latitude closed coronal loops in zones B, C, and F. However, for the case of the low-cadence bipole simulations, the latitudinal extend of the loops in zone F does not extend far enough north to be consistent with the observations. This disagreement is found only on the east limb, as the flux patterns on the west limb have mostly been captured during their central meridian passage. The success of the high-cadence data simulations in producing the latitudinal extend of the east limb closed loops illustrates the importance of incorporating new bipoles into the synoptic maps both pre- and post-central meridian, as is done in AFT. Those included post-central meridian in a previous rotation aid the accuracy of the simulation on the far side of the Sun and during the east limb transit onto the visible disk.

The final zone of comparison is zone D, where there are a nested set of faint and broad large-scale coronal loops in the plane of the limb. Three of the simulations shown in Figure 9 reproduce this structure. Both of the high- and low-cadence simulations that include hyperdiffusion (Figure 9(b) and (e)) fail to reproduce it. Instead, they produce a narrow structure that is nearly perpendicular to the plane of the limb or just low-lying arcades. As this disagreement occurs in both the high- and low-cadence data simulations, the disagreement can be attributed to the use of hyperdiffusion in the corona.

Finally, in three simulations (Figures 9(c), (d), and (f)), U-loop structures are found. These relate to magnetic flux ropes that have previously erupted (Mackay & van Ballegooijen 2006a; Yeates & Mackay 2009; Bhowmik & Yeates 2021). Due to the use of the magnetofrictional technique instead of full MHD (Pagano et al. 2013a, 2013b, 2018), any erupting flux ropes pass through the solar corona significantly more slowly than when full dynamic behavior is allowed. This has the consequence that its takes significantly longer for coronal field lines to reconfigure into a noneruptive state after the eruption, which leads to the presence of these U-loops.

Overall, when considering the noneruptive field lines in the plane of the limb, it is concluded that the simulations using the high-cadence data combined with either ideal coronal physics (Figure 9(d)) or coronal physics involving ohmic-diffusion (Figure 9(c)) produce the best comparison with the observations. In contrast, simulations using the low-cadence data or hyperdiffusion produce the worst comparison. It should, however, be noted that any differences between these simulations are significantly less than those found when considering other phenomena.

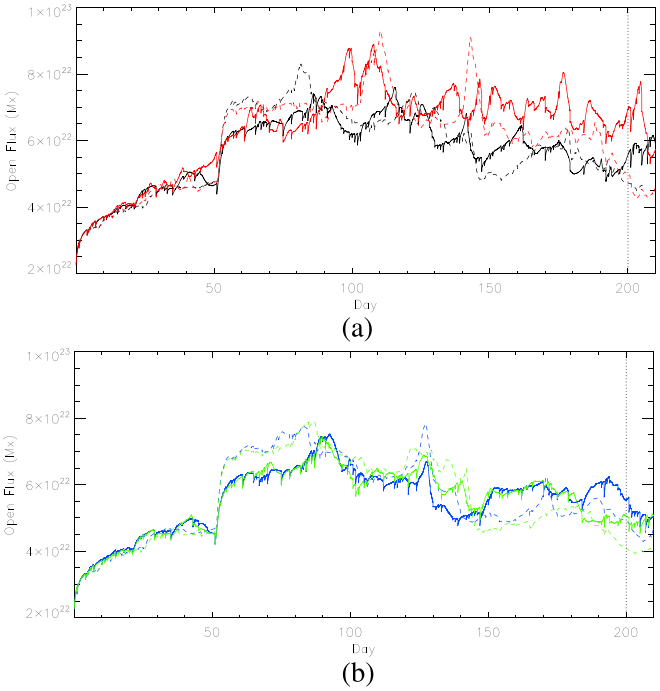

Figure 10. Graphs of the variation of the open flux as a function of time for (a) ideal (IdealA0 and IdealH0; shown in black) and supergranular helicity injection (SAHCA1 and SAHCH1, red) simulations and (b) simulations with ohmic dissipation (OhmA0 and OhmH0, green) and with hyperdiffusion (HDA0 and HDH0; shown in blue). In each graph, results are shown for the simulations using the high-cadence bipoles (solid lines) and low-cadence bipoles (dashed lines). For all of the simulations, the bipoles are inserted with zero twist. The vertical dashed line denotes the date of the eclipse.

3.5. Magnitude and Distribution of Open Flux

For the final set of comparisons, we will now consider how the magnitude and distribution of the open flux varies between the simulations. In each simulation, flux is regarded as open if it reaches $r = 2.5R_{\odot}$.

3.5.1. Magnitude of Open Flux

Figure 10 shows the variation of the open flux (Equation (13)) for the simulations where the bipoles twist parameter (β) is set to zero. Results are shown for (a) ideal

[5] Where the position angle is measured from the north pole in the counterclockwise direction.

(black lines) and SAHC (red lines) simulations and (b) hyperdiffusion (blue lines) and ohmic diffusion (green lines) simulations. Solid lines denote the simulations using the high-cadence bipoles and the dashed lines the low-cadence bipoles. As all simulations produce a similar level of open flux, the results are split across two separate graphs so that individual lines can be identified.

$$\Phi_o(t) = (2.5R_\odot)^2 \int_S |B_r(2.5R_\odot, \theta, \phi, t)| d\Omega \quad (13)$$

From Figure 10, it can be seen that all of the simulations follow a similar behavior. Initially, there is a rapid increase over the first 50 days, after which the open flux levels off, before decaying slightly toward the day of the eclipse (vertical dashed line). This variation is very similar to that seen for the surface flux. The initial enhancement in the open flux is a consequence of two effects. The first is the radial outflow velocity that is applied at the outer boundary, which leads to a small increase (see Rice & Yeates 2021). The second is the injection of electric currents into the coronal volume due to the large-scale consequences of differential rotation and flux emergence. This causes an inflation of the field and opening of previously closed field lines. During this ramp-up phase, all of the simulations present very similar results, where the magnitude of the open flux is not sensitive to the cadence of the bipoles nor the coronal physics in each simulation. After day 50, once the individual simulations form self-consistent non-potential configurations, they diverge slightly in their behavior. Numerous short-duration enhancements of open flux occur, where these enhancements represent flux ropes that lose equilibrium and are subsequently ejected from the simulation box (Bhowmik & Yeates 2021). Overall, the variation of the open flux shows few easily identifiable trends between the various simulations. The only significant difference is that the simulations involving supergranular helicity injection have more frequent and pronounced enhancements.

Figure 11 shows the amount of open flux on the day of the eclipse for all of the simulations given in Table 1. The symbols and colors are identical to those used in Figure 6. The solid horizontal line gives the 27-day average estimate of the open flux from OMNI centered around the day of the eclipse. The 27-day average is used to smooth out short-term local fluctuations. The black horizontal dashed or purple dashed–dotted lines that span the full length of the horizontal axis give the amount of open flux deduced from a PFSS model with source surface at $2.5R_\odot$, constructed using the surface configurations shown in Figures 4(b) and (c) for the high- and low-cadence bipole data sets respectively. For this comparison, we also include the additional results determined from PFSS extrapolations, as this method is the most common method used to determine the open flux (Wang & Sheeley 1995; Wang et al. 2000, 2002). This allows differences between the non-potential simulations and the PFSS approximation to be identified. As a further reference point, the open flux in the PFSS model is computed when the source surface is reduced (Asvestari et al. 2019; Linker et al. 2021) to $2.2R_\odot$ (plus symbols) or $2R_\odot$ (triangles) for both the high- and low-cadence data sets (black and purple respectively). The partial-length black dashed and purple dashed–dotted lines show the amount of open flux obtained when a PFSS model with source surface at $2.5R_\odot$ experiences the applied radial outflow velocity but with no additional lower-boundary driving. The effect of the radial outflow velocity is to increase the open flux by around

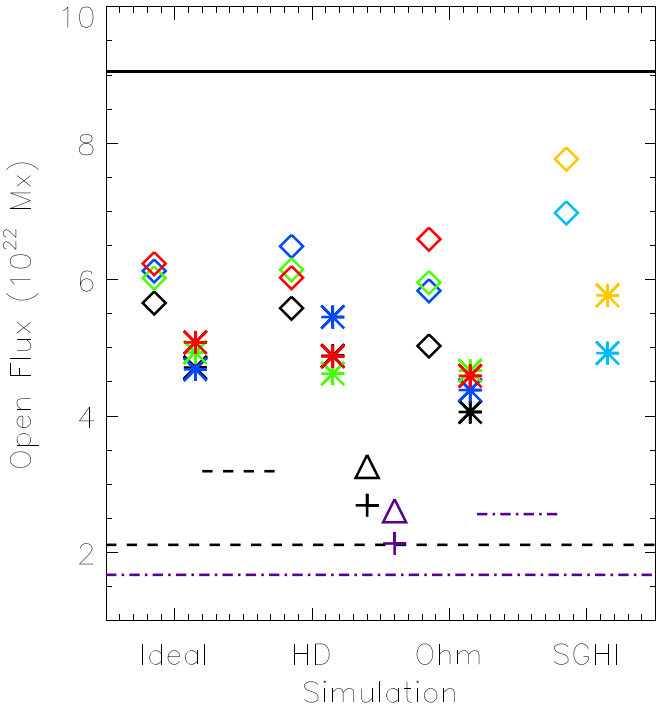

Figure 11. Scatter plots of the amount of open flux on 2015 March 20 for all of the simulations. The diamonds denote the simulations using bipoles determined from the high-cadence data set, while the stars denote the simulations using the low-cadence data set. Black color denotes a bipole twist parameter $\beta = 0$, blue $\beta = 0.2$, green $\beta = 0.4$, and red $\beta = 0.6$. The light blue and yellow colors denote a vorticity rate of 1×10^{-6} (light blue) and 5×10^{-6} (yellow). The solid horizontal line gives the OMNI 27-day average. The full length black/purple horizontal dash/dashed–dotted lines show the open flux deduced from a PFSS model with source surface at $2.5R_\odot$ for the high-/low-cadence data sets. Results for reducing the source surface of the PFSS model to either $2.2R_\odot$ (plus) or $2.0R_\odot$ (triangles) are also included for the high-cadence (black) and low-cadence (purple) data sets. The partial length black (high-cadence)/purple (low-cadence) horizontal dashed/dashed–dotted lines give the open flux deduced from a PFSS model ($2.5R_\odot$) when the radial outflow velocity is included.

50%. From this, it can be seen that neither lowering the source surface nor introducing the radial outflow velocity with the source surface at $2.5R_\odot$ produces an open flux equivalent to that found in the non-potential simulations or the 27-day averaged OMNI data.

It can be seen that the accuracy and complexity of the surface field does affect the amount of open flux in the PFSS extrapolation. On the day of the eclipse (day 200), the simulations using the high-cadence bipole data systematically have a slightly higher open flux than that found in the low-cadence simulations. In addition, as the bipole twist parameter or vorticity in the SAHC model increases, the amount of open flux also increases. Although each of the non-potential simulations have an open flux that is significantly higher than that deduced from the respective PFSS models, all of the simulations produce a value too low to explain the measured IMF (see Linker et al. (2017) for a discussion of the open flux problem where coronal models underestimate the heliospheric magnetic flux). The increased levels of open flux in the non-potential simulations are due to three main effects: (i) the applied radial outflow velocity representing the solar wind, (ii) a long-term enhancement as a consequence of the applied boundary driving motions injecting electric currents into the corona and inflating the coronal field, and (iii) sporadic enhancements as a consequence of flux rope ejections. Overall,

the enhancement due to injected electric currents produces the largest increase. A more detailed discussion of this can be found in the papers of Mackay & van Ballegooijen (2006a, 2006b) and Yeates et al. (2010).

Over all the simulations, the combination of SAHC and the high-cadence bipole data result in the closest match to the value found in the OMNI observations. In particular, the SAHC simulation with a vorticity of 5×10^{-6} s^{-1} produces an open flux of 7.8×10^{22} Mx. As the non-potential simulations produce significantly higher levels of open flux, it is important to quantify how much of this open flux is due to dislocated U-loops: examples of this can be seen in Figures 9(c), (d), and (f). In all 28 simulations, the amount of open flux that is dislocated is less than 2% of the total open flux for 27 out of 28 simulations. The only exception is simulation SAHCA1 (Figure 9(f)), where 4.5% of the open flux is dislocated. Even this higher value is low, and from this it can be seen that, in all of the non-potential simulations, the enhanced levels of open flux on the day of the eclipse are mainly due to open field lines rooted in the photosphere.

3.5.2. Distribution of Open Flux

While the results presented in Figures 10 and 11 demonstrate how the magnitude of open flux varies in the simulations, they do not provide any information on the distribution of open flux or radial magnetic field at $r = 2.5R_{\odot}$. It is found that on the day of the eclipse all of the non-potential simulations in Table 1 produce similar and consistent distributions of the radial magnetic field at $r = 2.5R_{\odot}$ as the bipole cadence, coronal physics, or helicity injection mechanisms are varied. Figure 12 shows a sample of the simulations to highlight what differences do arise. For this comparison, once again we include results determined from PFSS extrapolations, the most common method used to determine the open flux, so that differences between it and the non-potential simulations can be identified. Figures 12(a) and (b) show results from PFSS extrapolations, while panels (c)–(f) show results from the non-potential simulations. The left-hand panels show the high-cadence bipole simulations, while the right-hand panels show results from the same low-cadence simulation. Red/blue denotes positive/negative values of B_r, where in all panels the values saturate at ± 0.4 G, where the color bar on the right-hand side provides the scaling. The non-potential simulations in Figures 12 (c) and (d) are shown for the ohmic diffusion case with $\beta = 0.4$. In contrast, those in Figures 12 (e) and (f) use SAHC, where $\omega_l = 5 \times 10^{-5}$ s^{-1}. In all of the panels in Figure 12, the heliospheric current sheet, which divides regions of positive and negative B_r, has a complex shape and extends far into the southern hemisphere.

The PFSS extrapolations shown in Figures 12(a) and (b) are determined from the photospheric field distributions in Figures 4(b) and (c). Both produce distributions of the radial magnetic field at $r = 2.5R_{\odot}$ that have some similarities, but the low-cadence case is structurally much simpler. In both panels, the negative open flux is mainly concentrated around the southern polar region, but it has an extension into the northern hemisphere at 0° (or 360°) longitude. In contrast, the positive open flux is considerably weaker at the north pole, but strong values arise in the southern hemisphere around longitudes of 80° and 200°. While the two PFSS extrapolations have some degree of agreement, there are also two areas of significant difference. The first is that the positive polarity region around 80° longitude, is significantly stronger in the high-cadence data. The opposite occurs between 200° and 300° longitude, where in the low-cadence simulation there is a stronger and more extended positive region. These differences arise as a consequence of the low-cadence simulation missing bipoles and complexity of the field at locations 1–5 in Figure 4(a).

On comparing the non-potential simulations with the corresponding PFSS results, the non-potential simulations exhibit many of the same features found in the PFSS extrapolations. While similarities exist, the non-potential simulations produce stronger and more complex distributions. In Figures 12(c)–(f), the large negative open flux distribution increases in both size and strength. Furthermore, the positive open flux shows significant enhancements around $\phi = 80°$, $\lambda = -20°$, and between $\phi = 200°$ and 300°, $\lambda = -30°$. In addition to these enhancements, which are common to both the low- and high-cadence simulations, the high-cadence simulations have a number of additional positive and negative enhancements.

While there are no observations of the radial magnetic field at $r = 2.5R_{\odot}$ to compare to, the comparison of the various potential and non-potential simulations produces some interesting results. The first is that the potential and non-potential simulations produce significantly different distributions of open flux. While this is the case, the various non-potential simulations produce similar results. This arises because the open flux in the non-potential simulations depends mainly on surface motions injecting electric currents into the coronal field. This causes the field to expand and reach the outer boundary. The similarity between all of the non-potential simulations indicates that the photospheric flux distribution combined with the surface motions is more critical in determining the open flux compared to variations in the coronal physics. The only exceptions to this are the simulations that include SAHC, as doing so provides an additional small-scale injection of electric currents into the field, which further enhances the open flux. Due to this, it appears that a critical part in obtaining the open flux will be the accuracy of the photospheric field. Therefore, models such as AFT, which model as accurately as possible the surface field via emerging bipoles both pre- and post-central meridian, should be used instead of Carrington rotation maps to produce a representation of the open flux and HCS as accurately as possible. This applies whether the coronal models are potential or non-potential. Doing so is extremely important for solar wind models and space weather prediction.

Figure 13 shows the spatial distribution of the open and closed field lines at the solar photosphere ($r = R_{\odot}$) for the simulations shown in Figure 12. In each panel, closed regions are denoted by green, while open positive/negative regions are denoted by red/blue. The open and closed locations at the solar photosphere are determined by tracing field lines from $r = R_{\odot}$ and determining whether or not they hit the outer boundary at $r = 2.5R_{\odot}$. The number of field lines traced in both latitude and longitude is four times the respective number of grid points in each direction. The PFSS models constructed from both the high- and low-cadence bipole simulations (Figures 13 (a) and (b)) are in broad agreement. The southern hemisphere contains a large, open, negative-polarity region at the pole, which extends toward the equator. There is, however, a slight disagreement in the exact longitudes of this extension. In both cases, the northern hemisphere polar field is mostly closed. However, a number of thin and extended zones of positive

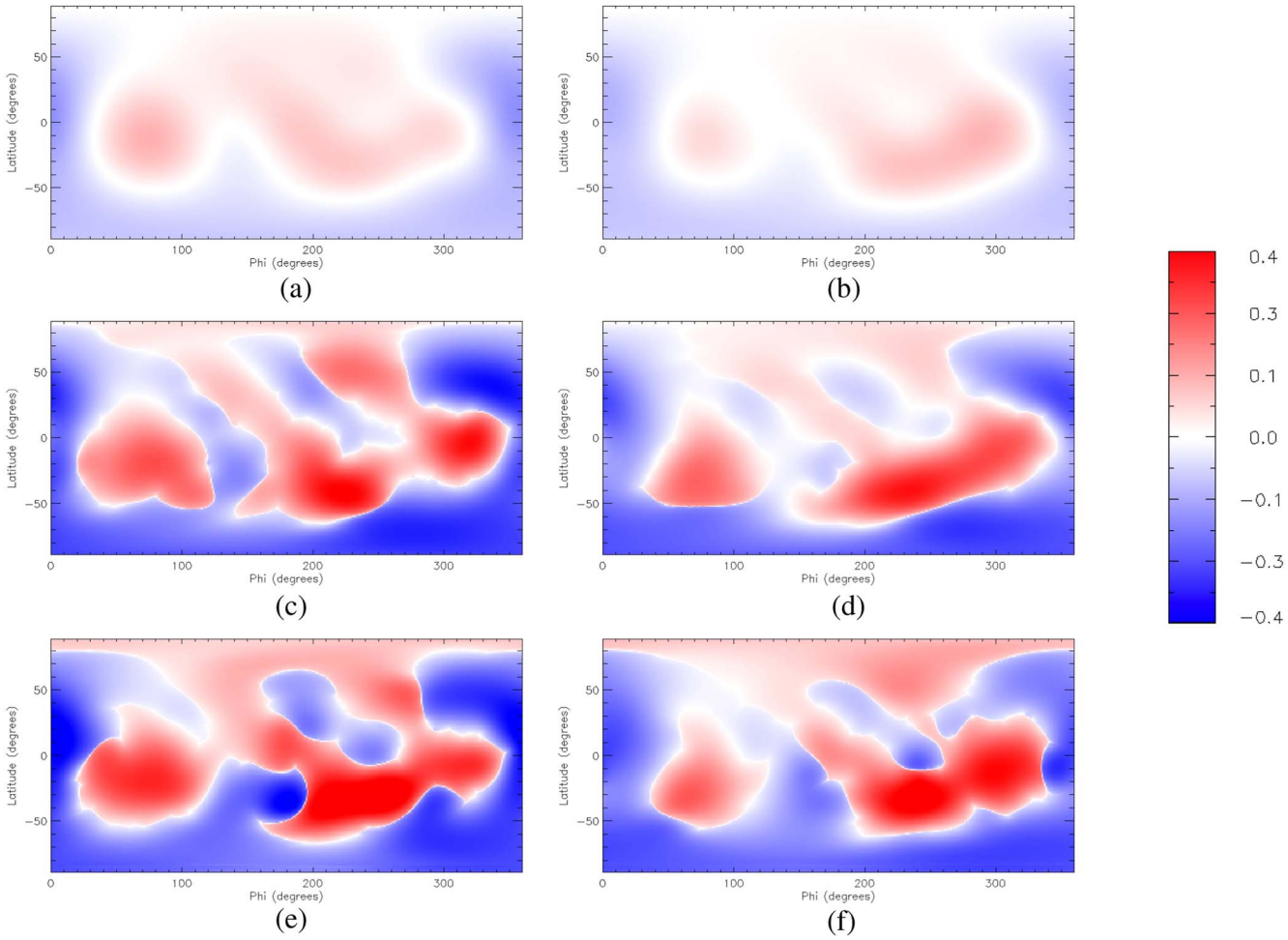

Figure 12. Distributions of the radial magnetic field (B_r) at 2.5 solar radii for a PFSS extrapolations (a and b) and non-potential simulations (c–f). The left/right-hand columns show results from the high/low-cadence bipole data sets. The middle row shows results from simulations (c) OhmA4 and (d) OhmH4, while the bottom row shows results from (e) SAHCA5 and (f) SAHCH5. In each plot, red/blue represents positive/negative B_r. The fields saturate at ± 0.4 G.

open flux exist between longitudes of $\phi = 50^\circ - 320^\circ$ in both hemispheres. The most notable difference between these high- and low-cadence cases occurs for the positive polarity at $\phi = 60^\circ$, $\lambda = -20^\circ$, where a different shape of the open footpoints arises. This is a consequence of the high-cadence simulation including stronger more complex polarities at location 1 shown in Figure 4(a).

Figures 13(c)–(f) show the distribution of the open footpoints for the non-potential cases seen in Figures 12(c)–(f). When non-potential effects are included, the distribution of the open footpoints at the photosphere is significantly more complex, where many additional small regions of both positive or negative polarity open footpoints arise across all latitudes. Many of the new open locations are rooted at the edges of strong flux concentrations. Due to this, they can provide a significant contribution to the open flux while remaining small in size. Due to their size, they are unlikely to appear as coronal holes. One difference between the non-potential simulations with and without SAHC is that, when SAHC is not included, there is limited open flux around the northern pole. When it is included, a large area of positive open flux is produced. This indicates that the small-scale injection of magnetic helicity across the solar surface over long periods of time can have a significant effect on the distribution of open flux at the solar photosphere (Antiochos 2013).

4. Summary & Conclusions

In this paper, we have considered the range and variety of solutions that can be produced by the global evolution model of Mackay & van Ballegooijen (2006a) and Yeates (2014) as the input data, coronal physics, and helicity injection mechanisms are varied. To carry out this comparison, all of the simulations are evolved forward in time, over the same time period, so that a comparison with observed coronal structures can be carried out on a fixed date. This date was chosen to be 2015 March 20, the date of the solar eclipse. This date was also chosen because it corresponds to the date used in the review paper of Yeates et al. (2018), which considered a variety of global models. This allows the range of solutions obtained here to be compared with the other models. To produce the simulated coronal field on this date, all of the simulations in the present paper start on 2014 September 1. By comparing the simulations in this way, we can determine how well the model reproduces specific phenomena found on the Sun, on a specific day. This approach is in contrast to previous studies using this model, which have considered general trends over time periods of months to years. In such studies, only one simulation run tends to be described in detail. While this provides important results, much information can still be gained from presenting less successful runs that use different physics, parameters, or input data. This is useful for guiding future applications of the model. Also,

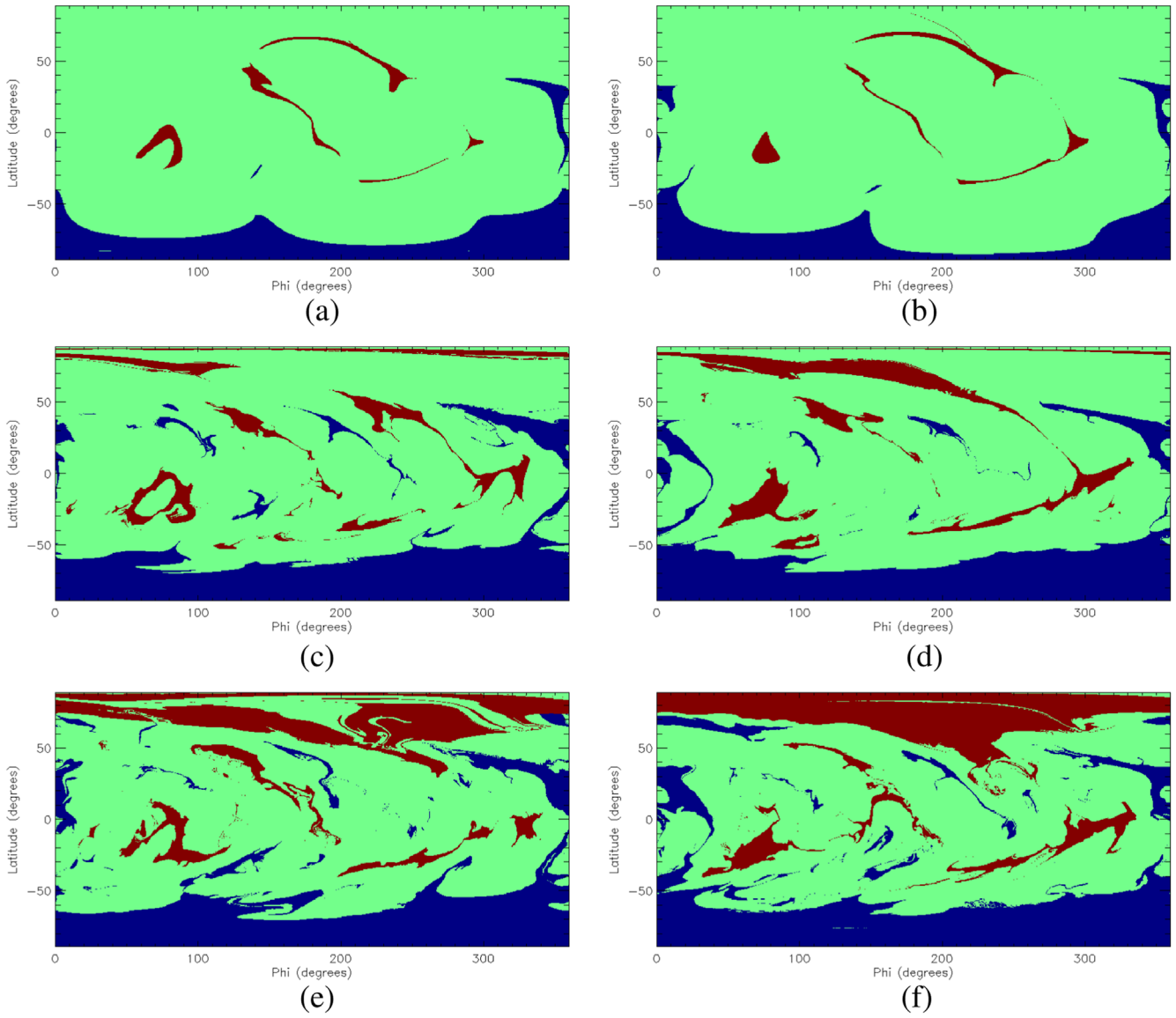

Figure 13. Distribution of open and closed field lines at the solar photosphere for PFSS extrapolations (a and b) and non-potential simulations (c–f). The left-/right-hand columns show results from the high-/low-cadence bipole data sets. The middle row shows results from simulations (c) OhmA4 and (d) OhmH4, while the bottom row shows results from (e) SAHCA5 and (f) SAHCH5. In each plot, red/blue represent positive/negative B_r open footpoints. The green locations represent closed field at the solar surface.

evaluating the accuracy of a model on a given date, relative to known coronal structures, is important to evaluate how well a model performs for space weather purposes (Pagano et al. 2018). This applies to both eruptive and noneruptive space weather phenomena.

With this in mind, the goal of the present paper is to evaluate the accuracy of the global magnetofrictional evolutionary models:

1. as the accuracy and cadence of the magnetograms used to determine new magnetic bipoles are varied;
2. to consider how the use of either the ideal assumption, ohmic diffusion, or hyperdiffusion in the corona affects the formation of non-potential coronal fields; and
3. to determine whether internal bipole helicity in emerging bipoles or helicity condensation best reproduces locations of non-potential fields.

Varying these three sets of parameters leads to a large number of possible combinations, especially when many of them may take a continuous range of values. To make the analysis manageable, we limited ourselves mostly to parameters previously found in published literature where 28 different simulations are compared. The comparison then considers: (i) the distribution of photospheric radial magnetic field and total flux, (ii) the total magnetic energy, (iii) volume-integrated electric current, (iv) solar filament locations, (v) limb structures, (vi) magnitude of open flux, (vii) radial magnetic field at $r = 2.5R_{\odot}$, and finally (viii) open footpoints at the solar photosphere.

Significant differences arise when deriving the bipole data from both the AFT (high-cadence) and SDO/HMI Carrington rotation (low-cadence) maps. In total, 197 new bipoles are identified from the AFT maps with a total flux of 2.1×10^{24} Mx. In contrast, when using the SDO/HMI Carrington rotation maps, only 110 bipoles are identified, with a total flux of

1.1×10^{24} Mx. As a consequence, the simulations using the high-cadence data produce significantly higher flux values and more complex distributions. In addition, the simulations using the high-cadence data produce more accurate distributions of surface flux at the east limb and as the flux rotates toward the central meridian. This arises as, in the high-cadence maps, new bipoles are included both pre- and post-central meridian. In contrast, in the Carrington rotation maps, they are only included at the central meridian. This has important consequences for reproducing solar filaments both near the limb and pre-central meridian (Figure 8) and also for producing the correct latitudinal extend of arcades from low-latitude active regions at the east limb (Figure 9; see also Meyer et al. 2020).

Another consequence of using the high-cadence bipole data derived from AFT maps to drive the simulations is that significantly higher magnetic energies and electric currents are produced compared to using standard Carrington rotation maps. This leads to greater non-potentiality in the corona, which is important for explaining eruptions. Also in the high-cadence simulations, higher values for the open flux arise; however, these values are still significantly below the values measured from OMNI, which will be discussed in more detail below. Another important distinction between the high- and low- cadence simulations is the distribution of open flux that is produced at $r = R_{\odot}$ and $r = 2.5R_{\odot}$. A number of differences arise in both magnitude and distribution both for PFSS models and non-potential models. Such differences may be important for producing accurate distributions of the solar wind to be used as boundary conditions for Space Weather models such as ENLIL. Due to this, future studies should consider whether coronal fields produced from AFT data provide a better fit compared with observations compared to either daily or Carrington rotation maps.

One of the first comparisons carried out in the paper was with solar filaments observed in BBSO/Hα images. This considered how well the various simulations produce sheared non-potential fields along PILs at the observed locations of solar filaments. In this comparison, it is found that the coronal physics and helicity injection mechanisms played a more significant role than the cadence of the bipole data. However, when the low-cadence bipole data were, used they failed to produce all of the PILs at the correct locations. Simulations using hyperdiffusion produced the worst fit on the day of the eclipse, where it inhibited the formation of strong localized electric currents along the PILs. Both ideal or ohmic-diffusion simulations produce very similar results as additional helicity is injected through the optional bipole twist parameter. Optimal results occur for β in the range 0.2–0.4, where values outside this range introduce either too little or too much twist to match the observations on this given day. When including SAHC, a similar result occurs whereby a vorticity of 1×10^{-6} s^{-1} produces better results than 5×10^{-6} s^{-1}. Optimal values arise as, when either mechanism is too high, the sheared fields and flux ropes form too quickly to match the observed structures on the given day and are ejected, leaving only weakly sheared fields behind. This illustrates the importance of comparing all of the simulations on a given day rather than just comparing monthly averages. Overall, it is found that the ohmic diffusion simulation using $\beta = 0.4$ is the only simulation that reproduces all of the observed filaments, and as such gives the best fit. It is difficult to distinguish the other ideal, ohmic-diffusion, or SAHC simulations from each other, as they produce similar results. This provides some robustness to the results, as these terms are varied. However, it is clear that hyperdiffusion leads to the worst comparison with the filament observations where it inhibits the formations of sheared arcades or flux ropes. This result appears to be in contradiction to that found in Bhowmik & Yeates (2021), as they found that, when using hyperdiffusion, slightly more flux rope ejections occurred compared to when using ohmic diffusion, even though similar rates and forms are used in both papers. The difference is likely due to the fact that the papers are considering different phases of the solar cycle. For the present paper, it is during high activity in cycle 24 when significant numbers of bipoles are emerging and producing strong localized gradients in the field and subsequently in α. Due to these gradients, hyperdiffusion has a significant effect in trying to smooth them out. In contrast, Bhowmik & Yeates (2021) considered a period during the deep minimum of cycle 24, where they discarded any new emerging regions. Due to this, in the simulations of Bhowmik & Yeates (2021), the gradients in the field are continually decreasing, leading to a more uniform distribution wherein the effect of hyperdiffusion is reduced. This indicates that care should be taken when using hyperdiffusion to simulate the formation of filament channels or flux ropes.

The variation of the results produced by the simulations is significantly less when considering structures observed at the solar limb. For this comparison, field lines at the limb were compared to a SWAP 174 Å image. In contrast to what was found for solar filaments, the high-cadence bipole simulations determined from AFT now produce a better agreement, in particular at the east limb. This is a consequence of bipoles being identified and emerged post-central meridian, before they rotate off the west limb. They then rotate back into view 13 days later at the east limb and produce the correct latitudinal extent of the arcades at the limb. As discussed previously, as the twist of the bipoles or the rate of SAHC is varied, only small variations in the limb structures arise. This indicates that the limb structures are not sensitive to these quantities. In contrast, varying the coronal physics does have an effect. Simulations using either ideal or ohmic-diffusion assumptions produce equally consistent results with the observations for the nonerupting structures. However, hyperdiffusion in both the high- and low-cadence simulations fails to reproduce the large, diffuse arcade seen at location D in Figure 9(a).

For the open flux, all of the non-potential simulations produce significantly higher levels of open flux compared to the PFSS models. While this significantly reduces the discrepancy between values determined at the Sun and those computed at 1AU from OMNI data, it does not account for all of the differences. However, as shown in Rice & Yeates (2021), if a stronger outflow is used (150–400 kms^{-1}), then the discrepancy may also be reduced. Future studies should consider by how much the outflow speeds required in Rice & Yeates (2021) can be reduced if non-potential effects such as helicity condensation are included. In addition to the effects occurring in the low corona, it is also likely that interplanetary/solar wind effects are also overestimating the strength of B_r measured at 1AU (Owens et al. 2017). In the non-potential simulations, the reduced discrepancy is due to (i) an enhancement in the open field regions found in PFSS models, which are mostly located at high latitudes, and (ii) the generation of new open regions at low latitudes. While the open regions at low latitudes are small, they are located in

strong field regions and can contribute a significant amount to the open flux. Once again, it is found that the simulations using the high-cadence bipoles produce results more consistent with the observations than those using the low-cadence bipoles. The coronal physics applied has little effect on the amount of open flux, where it is difficult to differentiate between the simulations. In contrast, as the non-potential injection parameters for both bipole twist and SAHC are increased, higher values of open flux are found. Overall, the combination of the high-cadence bipoles and SAHC produces the highest values of open flux. This indicates that the continual small-scale injection of helicity across the Sun can have a significant effect on the strength of interplanetary magnetic field. While it is beyond the scope of the present study, in a future study we will consider the variation of open flux footpoints as a function of time, throughout the entire duration of the simulations, and compare this to EUV observations of coronal holes.

The main aim of the present paper has been to quantify the range and variability of solutions that can be found using the global evolutionary magnetofrictional model as the input data, helicity injection mechanisms, and coronal physics are varied. While this has been the main aim, it is also important to quantify these solutions in terms of the results presented in Yeates et al. (2018). Although it is not possible to compare each of the solutions presented in the present paper with the range of solutions found in Yeates et al. (2018), some general conclusions can be drawn. Yeates et al. (2018) found that there was significant disagreement in the structure of the magnetic field found between the models. This disagreement was attributed to the use of different input data, modeling techniques, and outer boundary conditions. While a range of solutions have been found for the evolving magnetofrictional model, all model runs have produced qualitatively the same features, relative to the models in Yeates et al. (2018). However, the exact quantitative results vary depending on input data, helicity injection mechanisms, and coronal physics. The key aspect is that the evolving magnetofrictional model with the evolving lower boundary condition is able to naturally energize the global coronal both at low and high latitudes. This property is a key element in being able to represent large-scale filament channels, filaments, and coronal loops.

While the evolutionary magnetofrictional model has produced qualitatively the same results, the present study has allowed us to more fully understand why the model performed the way it did in Yeates et al. (2018). First of all, the use of AFT data as done in Yeates et al. (2018) to determine the bipole data sets makes the model significantly more energized and accurate, compared to using Carrington rotation synoptic maps (Yeates et al. 2008). In terms of the ratio of total magnetic energy to potential field magnetic energy, a range of values can be found from 1.12 to 1.9. Including hyperdiffusion leads to the lowest ratios, and SAHC to the highest ratio. The values obtained in the present paper span the full range of values found in Table 2 of Yeates et al. (2018).

While the magnetofrictional result presented in Yeates et al. (2018) used the same ohmic diffusion and bipole helicity injection parameters as simulation OhmA4, the results presented here show that similar solutions can be found when applying the SAHC model of Antiochos (2013) or ideal corona physics. While similar results can be found, the parameters and physics used in OhmA4 tend to lead to the best result overall when comparing to solar filaments and limb structures. It was not by chance that these parameters were used in the magnetofrictional simulation in Yeates et al. (2018), as they had previously been used in Yeates et al. (2008) when modeling the chirality and formation of filament channels. However, if hyperdiffusion had been used instead in the magnetofrictional simulation of Yeates et al. (2018), the simulation would have performed significantly worse relative to the other models.

Finally, the present paper has shown that significantly higher levels of open flux, compared to the solutions provided in Yeates et al. (2018), can be found. These values are more consistent with the measured IMF field strength and can be produced using higher bipole twist values or with SAHC. Although higher values are found, the values are still too low, and future studies need to compare the open footpoints at the solar surface with coronal hole data for consistency and discrepancies.

From the results described above, it is clear that, as the cadence of the bipole data, coronal physics, and helicity injection mechanisms are varied, results consistent with the observations can be found. While this is the case, use of low-cadence data determined from 27-day Carrington rotation synoptic maps or hyperdiffusion in the corona leads to the worst agreement with the observations on this given day. As such, future studies should take care when using either or both of these in simulations. Using them leads to significantly lower energies and electric currents, as well as less production of sheared fields and flux ropes along PILs. This is likely to limit the accuracy of these simulations in building up and storing free magnetic energy to explain eruptions. In contrast, using high-cadence data such as those derived from AFT maps, combined with either ideal approximations or ohmic diffusion, leads to the best comparison with the observations. This is true for both the on-disk non-potential structures and the off-limb near-potential structures.When coupled with helicity injection mechanisms such as bipole self-twist or SAHC, it can reproduce both low-lying non-potential structures such as solar filaments and larger-scale near-potential limb structures. Optimal values of these parameters lie in the range $\beta = 0.2$–0.4 or 1×10^{-6} s^{-1}, where in the present study it is difficult to distinguish between these mechanisms.

The quantity that depends the least on the coronal physics is the magnitude and distribution of open flux. While this is the case, significant difference in the open flux can be found: (i) as the cadence of the bipole data is varied, (ii) if potential or non-potential models are applied, and (iii) if additional helicity injection mechanisms are included. It is interesting to note that, even for the simplest coronal field of a PFSS model, the increased accuracy of the photospheric boundary condition produced by AFT leads to a number of variations in the strength and distribution of open flux at $r = 2.5R_{\odot}$.

While the present paper has compared the variety of solutions that can be produced from the global magnetofrictional evolutionary model of Mackay & van Ballegooijen (2006a) and Yeates (2014), there are still a number of phenomena that can be considered in future studies. The present investigation has mainly focused on noneruptive phenomena in the solar corona. However, it still needs to be determined how well each simulation reproduces both the location and timing of eruptions throughout the duration of the simulation as the various input data, mechanisms, and parameters are varied (Bhowmik & Yeates 2021). Such an

extensive study of all 28 simulations is not possible in the present paper, but this will be considered in a future study. Such a comparison will be made over the entire 210 days of the simulations, not just on a single day as considered here. The next study relates to the distribution and strength of the open flux in both the PFSS models and non-potential models. It is clear that non-potential models can produce significantly enhanced open flux both at the solar photosphere and at $r = 2.5R_{\odot}$. To consider how these distributions arise from those found in the initial condition, the evolution of open flux over the entire time period of the simulation needs to be analyzed. Such a study will then be able to determine how and where the open field regions depart from coronal holes seen in EUV. While such a comparison with coronal holes is useful, care must be taken when comparing coronal holes to simulations, as not all open field regions have to originate within coronal holes (Linker et al. 2017). Next, as shown in Figure 12, even for PFSS models, the simplest approximation produce significantly different results for the distribution of B_r as the accuracy of the photospheric field increases. Due to this, it would be interesting to consider how the increased accuracy in the AFT maps affects the solar wind boundary conditions produced for models such as ENLIL.

D.H.M. would like to thank the STFC for support via consolidated grant ST/N000609/1, as well as the Leverhulme Trust for financial support. L.A.U. was supported by the NASA Living With a Star program (NNH16ZDA010N-LWS) and by the National Science Foundation Atmospheric and Geospace Sciences Postdoctoral Research Fellowship Program (Award #1624438). The authors thank the International Space Science Institute in Bern, Switzerland, for hosting a team on Global Non-Potential Magnetic Models of the Solar Corona, led by A. Yeates, where some of the ideas were developed. SWAP is a project of the Centre Spatial de Liège and the Royal Observatory of Belgium funded by the Belgian Federal Science Policy Office (BELSPO). The authors are grateful to the SDO/HMI and SWAP teams for the data, which was obtained through the Joint Science Operations Centre (JSOC: jsoc.stanford.edu). SWAP data preparation routines were used within SolarSoft IDL (www.lmsal.com/solarsoft/. BBSO operation is supported by NJIT and US NSF grant AGS-1821294. GST operation is partly supported by the Korea Astronomy and Space Science Institute, the Seoul National University, and the Key Laboratory of Solar Activities of Chinese Academy of Sciences (CAS) and the Operation, Maintenance, and Upgrading Fund of CAS for Astronomical Telescopes and Facility Instruments.

ORCID iDs

Duncan H. Mackay https://orcid.org/0000-0001-6065-8531

References

Altschuler, M. D., & Newkirk, G. 1969, SoPh, 9, 131
Amari, T., Aly, J. J., Canou, A., & Mikic, Z. 2013, A&A, 553, A43
Antiochos, S. K., Dahlburg, R. B., & Klimchuk, J. A. 1994, ApJL, 420, L41
Antiochos, S. K. 2013, ApJ, 772, 72
Asvestari, E., Heinemann, S. G., Temmer, M., et al. 2019, JGRA, 124, 8280
Aulanier, G., & Demoulin, P. 1998, A&A, 329, 1125
Badman, S. T., Bale, S. D., Martinez Oliveros, J. C., et al. 2020, ApJS, 246, 23
Bhowmik, P., & Yeates, A. R. 2021, SoPh, 296, 109
Bhattacharjee, A., & Yuan, Y. 1995, ApJ, 449, 739
Bogdan, T. J., & Low, B. C. 1986, ApJ, 306, 271
Bommier, V., Degl'Innocenti, E. L., Leroy, J.-L., & Sahal-Br?chot, S. 1994, SoPh, 154, 231
Boozer, A. H. 1986, JPlPh, 35, 133
Contopoulos, I., Kalapotharakos, C., & Georgoulis, M. K. 2011, SoPh, 269, 351
Contopoulos, I. 2013, SoPh, 282, 419
DeVore, C. R., & Antiochos, S. K. 2000, ApJ, 539, 954
Duvall, T. L. 1979, SoPh, 63, 3
Feng, X., Yang, L., Xiang, C., et al. 2012, SoPh, 279, 207
Gaizauskas, V. 1998, in ASP Conf. Ser. 150, IAU Coll. 167: New Perspectives on Solar Prominences, ed. D. F. Webb, B. Schmieder, & D. M. Rust (San Francisco, CA: ASP), 257
Gibb, G. P. S., Mackay, D. H., Green, L. M., & Meyer, K. A. 2014, ApJ, 782, 71
Gibson, S. E., & Fan, Y. 2006, JGRA, 111, A12103
Hoeksema, J. T., Abbett, W. P., Bercik, D. J., et al. 2020, ApJS, 250, 28
Karna, N., Savcheva, A., Gibson, S., et al. 2021, ApJ, 913, 47
Kazachenko, M. D., Fisher, G. H., & Welsch, B. T. 2014, ApJ, 795, 17
Kazachenko, M. D., Fisher, G. H., Welsch, B. T., Liu, Y., & Sun, X. 2015, ApJ, 811, 16
Kuperus, M., & Raadu, M. A. 1974, A&A, 31, 189
Labrosse, N., Heinzel, P., Vial, J. C., et al. 2010, SSRv, 151, 243
Leighton, R. B. 1964, ApJ, 140, 1547
Linker, J. A., Caplan, R. M., Downs, C., et al. 2017, ApJ, 848, 70
Linker, J. A., Heinemann, S. G., Temmer, M., et al. 2021, ApJ, 918, 21
Lumme, E., Pomoell, J., & Kilpua, E. K. J. 2017, SoPh, 292, 191
Mackay, D. H., & van Ballegooijen, A. A. 2001, ApJ, 560, 445
Mackay, D. H., & van Ballegooijen, A. A. 2006a, ApJ, 641, 577
Mackay, D. H., & van Ballegooijen, A. A. 2006b, ApJ, 642, 1193
Mackay, D. H., Karpen, J. T., Ballester, J. L., Schmieder, B., & Aulanier, G. 2010, SSRv, 151, 333
Mackay, D. H., Green, L. M., & van Ballegooijen, A. 2011, ApJ, 729, 97
Mackay, D. H., DeVore, C. R., & Antiochos, S. K. 2014, ApJ, 784, 164
Mackay, D. H., Yeates, A. R., & Bocquet, F.-X. 2016, ApJ, 825, 131
Mackay, D. H., DeVore, C. R., Antiochos, S. K., et al. 2018, ApJ, 869, 62
Meyer, K. A., Mackay, D. H., Talpeanu, D.-C., Upton, L. A., & West, M. J. 2020, SoPh, 295, 101
Mikic, Z., & Linker, J. A. 1994, ApJ, 430, 898
Mikic, Z., Linker, J. A., Schnack, D. D., Lionello, R., & Tarditi, A. 1999, PhPl, 6, 2217
Mikic, Z., Downs, C., Linker, J. A., et al. 2018, NatAs, 2, 913
Owens, M. J., Lockwood, M., Riley, P., & Linker, J. 2017, JGRA, 122, 10980
Pagano, P., Mackay, D. H., & Poedts, S. 2013a, A&A, 554, A77
Pagano, P., Mackay, D. H., & Poedts, S. 2013b, A&A, 560, A38
Pagano, P., Mackay, D. H., & Yeates, A. R. 2018, JSWSC, 8, A26
Pomoell, J., & Poedts, S. 2018, JSWSC, 8, A35
Rice, O. E. K., & Yeates, A. R. 2021, ApJ, 923, 57
Rust, D. M., & Kumar, A. 1994, SoPh, 155, 69
Schatten, K. H., Wilcox, J. M., & Ness, N. F. 1969, SoPh, 6, 442
Schatten, K. H. 1971, CosEl, 2, 232
Scherrer, P. H., Schou, J., Bush, R. I., et al. 2012, SoPh, 275, 207
Sheeley, N. R. 2005, LRSP, 2, 5
Snodgrass, H. B. 1983, ApJ, 270, 288
Strauss, H. R. 1988, ApJ, 326, 412
Taylor, J. B. 1974, PhRvL, 33, 1139
Upton, L., & Hathaway, D. H. 2014a, ApJ, 780, 5
Upton, L., & Hathaway, D. H. 2014b, ApJ, 792, 142
van Ballegooijen, A. A., Priest, E. R., & Mackay, D. H. 2000, ApJ, 539, 983
van Ballegooijen, A. A., & Mackay, D. H. 2007, ApJ, 659, 1713
Virtanen, I., & Mursula, K. 2016, A&A, 591, A78
Wagner, A., Asvestari, E., Temmer, M., Heinemann, S. G., & Pomoell, J. 2022, A&A, 657, A117
Wang, Y. M., & Sheeley, N. R. 1995, ApJL, 447, L143
Wang, Y.-M., Sheeley, N. R., & Lean, J. 2000, GeoRL, 27, 621
Wang, Y. M., Sheeley, Jr, N. R., & Lean, J. 2002, ApJ, 580, 1188
Weinzierl, M., Yeates, A. R., Mackay, D. H., Henney, C. J., & Arge, C. N. 2016, ApJ, 823, 55
Wiegelmann, T. 2007, SoPh, 240, 227
Wiegelmann, T., Neukirch, T., Nickeler, D. H., & Chifu, I. 2020, SoPh, 295, 145
Yang, W. H., Sturrock, P. A., & Antiochos, S. K. 1986, ApJ, 309, 383
Yardley, S. L., Pagano, P., Mackay, D. H., & Upton, L. A. 2021, A&A, 652, A160
Yardley, S. L., Mackay, D. H., & Green, L. M. 2021, SoPh, 296, 10
Yeates, A. R., Mackay, D. H., & van Ballegooijen, A. A. 2008, SoPh, 247, 103
Yeates, A. R., & Mackay, D. H. 2009, ApJ, 699, 1024

Yeates, A. R., Mackay, D. H., van Ballegooijen, A. A., & Constable, J. A. 2010, JGRA, 115, A09112
Yeates, A. R., & Mackay, D. H. 2012, ApJL, 753, L34
Yeates, A. R. 2014, SoPh, 289, 631
Yeates, A. R., Amari, T., Contopoulos, I., et al. 2018, SSRv, 214, 99
Yeates, A. R. 2020, SoPh, 295, 119